



A mid-Proterozoic coupled Sr and Li isotope excursion and its potential connection to enhanced weathering and ocean oxygenation at 1.57 Ga

Xi Chen^{a,b,*} , Ying Zhou^{a,c}, Simon W. Poulton^d , Fred T. Bowyer^e, Colin Mettam^a, Shihong Zhang^f, Maoyan Zhu^{g,h} , Da Liⁱ, Philip A.E. Pogge von Strandmann^{a,c}, Benjamin J.W. Mills^d , Graham A. Shields^a 

^a LOGIC, Department of Earth Sciences, University College London, London, UK

^b School of Ocean and Earth Science, University of Southampton, Southampton, UK.

^c MIGHTY, Institute of Geosciences, Johannes Gutenberg University, Mainz, Germany

^d School of Earth and Environment, University of Leeds, Leeds LS2 9JT, UK

^e School of Geosciences, University of Edinburgh, Edinburgh, UK

^f State key Laboratory of Biogeology and Environmental Geology, China University of Geosciences, Beijing, China

^g State Key Laboratory of Palaeobiology and Stratigraphy, Nanjing Institute of Geology and Palaeontology, Chinese Academy of Sciences, Nanjing, China

^h College of Earth and Planetary Sciences, University of Chinese Academy of Sciences, Beijing, China

ⁱ School of Marine Science and Engineering, Nanjing Normal University, Nanjing, China

ARTICLE INFO

Editor: Dr Tristan Horner

Keywords:

Sr isotopes
Li isotopes
Mesoproterozoic
Weathering
Oxygenation
Biological evolution

ABSTRACT

Chemical weathering is a critical Earth system process that regulates climate, ocean chemistry and the long-term carbon cycle. However, the intensity and variability of chemical weathering remain insufficiently constrained for the mid-Proterozoic (~1.8–0.8 Ga), greatly limiting our understanding of the environmental context to early eukaryotic evolution. Here, we report the first coupled positive seawater $^{87}\text{Sr}/^{86}\text{Sr}$ (~0.0007) and $\delta^7\text{Li}$ (~5‰) isotope excursions of the Mesoproterozoic Era (1.6–1.0 Ga), which we argue signifies a substantial weathering event at ~1.57 Ga, characterised by increased silicate weathering rates and decreased weathering congruency. Drawing on independent geological evidence, we posit that enhanced volcanic CO_2 degassing, possibly alongside accretional orogenesis, increased denudation rates and invigorated the hydrological cycle, amplifying silicate weathering and secondary clay formation. This weathering pulse broadly coincided with coeval ocean oxygenation and carbon cycle disruption, implicating it in the appearance of the earliest known decimetre-scale, multicellular eukaryotic fossils.

1. Introduction

Chemical weathering of silicate minerals sequesters CO_2 and drives marine carbonate precipitation by increasing the supply of dissolved cations and alkalinity to the oceans (Walker et al., 1981; West et al., 2005). Chemical weathering also provides critical nutrients (Fe, P, Si, etc.) to the coastal oceans, thereby promoting primary productivity (Berner, 2003). Therefore, understanding the dynamics of weathering conditions and their controlling factors is crucial to deciphering past changes to global climate, the carbon cycle, redox conditions and biological evolution. The mid-Proterozoic (1.8–0.8 Ga) has been long recognised as a time of unusually muted variability in terms of climate (Holland, 2006), tectonics (Cawood and Hawkesworth, 2014) and

ocean-atmosphere composition (Bartley and Kah, 2004; Brasier and Lindsay, 1998; Shields and Veizer, 2002). However, as more data have accumulated, this traditional view has been increasingly revised. Recent studies highlight that the Mesoproterozoic was considerably more dynamic than previously thought, marked by widespread orogenesis (Condie, 2021; Gervais et al., 2023), repeated emplacement of large igneous provinces and associated environmental disturbances (Diamond et al., 2021; Zhang et al., 2025), carbon isotope variability and fluctuations in surface redox conditions (Canfield et al., 2018; Luo et al., 2025), and key steps in early eukaryotic evolution (Brocks et al., 2023; Zhu et al., 2016). Despite these advances, Mesoproterozoic weathering regimes remain poorly constrained, limiting our understanding of its role in environmental change and biological innovation during Earth's

* Corresponding author.

E-mail address: Xi.Chen@soton.ac.uk (X. Chen).

<https://doi.org/10.1016/j.epsl.2026.119848>

Received 20 May 2025; Received in revised form 13 December 2025; Accepted 10 January 2026

Available online 16 January 2026

0012-821X/© 2026 The Authors. Published by Elsevier B.V. This is an open access article under the CC BY license (<http://creativecommons.org/licenses/by/4.0/>).

“middle age”. One factor that has hampered investigation of Mesoproterozoic weathering is a scarcity of high-quality weathering proxy records (Chen et al., 2022b; Kalderon-Asael et al., 2021), such as Sr ($^{87}\text{Sr}/^{86}\text{Sr}$) and Li ($\delta^7\text{Li}$) isotope ratios. Marine carbonate Sr and Li isotope records can represent robust archives of the Sr and Li isotope composition of ambient seawater, and in combination, have been successfully applied to constrain past weathering behaviour and climate change (Cao et al., 2022; Caves Rugenstein et al., 2019; Pogge von Strandmann et al., 2013).

Strontium and Li isotopes are homogeneously distributed in seawater on a global scale, due to their much longer modern ocean residence times ($\sim 10^6$ years) relative to the time it takes for oceans to circulate ($\sim 10^3$ years) (Elderfield, 1986; Huh et al., 1998). The Sr isotope budget of seawater is normally used to trace the relative importance of more radiogenic riverine input versus less radiogenic hydrothermal input (Spooner, 1976), but its interpretation is complicated by the large isotopic range of lithologies undergoing weathering (Bataille et al., 2017; Halverson et al., 2010; Peucker-Ehrenbrink and Fiske, 2019). Strontium isotopes in seawater are incorporated into carbonate minerals through substitution for calcium, without isotopic fractionation (McArthur, 1994).

By contrast, riverine $\delta^7\text{Li}$ values are largely independent of the silicate lithology being weathered, and not affected by weathering of carbonates, but the formation of silicate secondary minerals preferentially consumes ^6Li , driving residual waters to heavier isotopic values. Thus, riverine $\delta^7\text{Li}$ provides direct information on silicate weathering congruency, reflecting the extent of primary rock dissolution relative to secondary mineral formation (Misra and Froelich, 2012; Pogge von Strandmann and Henderson, 2015), and may also be a tracer for weathering intensity, reflecting the ratio of weathering rate (W) to the denudation rate (D) (Dellinger et al., 2015). The ocean Li reservoir is mainly sourced from riverine and hydrothermal inputs, while the oceanic sinks of Li primarily consist of uptake by low-temperature clays formed during the alteration of oceanic crust (AOC) and the formation of marine aluminous authigenic clays (MAAC) (Chan et al., 1992; Misra and Froelich, 2012). The incorporation of oceanic Li into authigenic clay minerals, a process known as reverse weathering, imparts a combined fractionation effect of $\sim 14\text{--}16\%$, which drives modern seawater to $\sim 31\%$ (Misra and Froelich, 2012). Seawater lithium isotope compositions ($\delta^7\text{Li}_{\text{sw}}$) can therefore be used to examine silicate weathering regimes and marine reverse weathering, thus complementing the $^{87}\text{Sr}/^{86}\text{Sr}_{\text{sw}}$ record. However, Mesoproterozoic marine carbonate $\delta^7\text{Li}$ data remain extremely sparse. Although recent studies have measured Li isotopes in ~ 1.4 Ga Xiamaling shales (Liu et al., 2025; Zhang et al., 2025) indicating more variable silicate weathering during this interval, coupled marine carbonate Li and Sr isotope records, necessary for reconstructing global seawater signals, are still largely lacking for the Mesoproterozoic.

The marine carbonate succession of the ~ 1.57 Ga Gaoyuzhuang (GYZ) Formation provides a unique opportunity to fill this gap. This succession hosts a negative carbon isotope excursion (CIE), with multiple geochemical proxies suggesting a contemporaneous marine oxygenation event (Luo et al., 2020, 2025; Shang et al., 2019; Song et al., 2024; Tang et al., 2022; Xie et al., 2023; Xu et al., 2023; Yang et al., 2025; Zhang et al., 2018) linked to the appearance of decimetre-scale, multicellular eukaryotic microfossils (Zhu et al., 2016). Here, we report $^{87}\text{Sr}/^{86}\text{Sr}$ and $\delta^7\text{Li}$ isotope ratios for marine carbonate rocks of the GYZ Formation, to reconstruct the weathering regime across this oxygenation event. We then utilise a geochemical box model to explore the driving mechanisms behind the weathering regime shift we document. Combined with published redox proxies, we subsequently consider plausible links between tectonics, climate, weathering, redox and biological evolution during the early Mesoproterozoic Era.

2. Geological setting

The Gaoyuzhuang Formation (GYZ) is located in the Yanliao Basin of the North China Craton (Fig. 1a). The GYZ interval marks the peak of marine transgression in the basin, during which a broad epeiric sea with connection to the open ocean developed (Zhang et al., 2018). From the GYZ to the overlying Wumishan Formation, up to ~ 5.7 km of carbonate strata accumulated, being thickest in the Jixian area (Zhang et al., 2018). The GYZ Formation corresponds to a period during the final assembly of the supercontinent Nuna, marked by accretion on its periphery, while extensional processes may have influenced its interior (Pourteau et al., 2018; Zhang et al., 2012). In ascending order, the GYZ Formation can be divided into four members Member I (Guandi Member), Member II (Sangshu'an Member), Member III (Zhangjiayu Member) and Member IV (Huanxiusi Member). This study focuses on GYZ Member III, which consists mainly of limestone and dolomitic limestone deposited during a transgression-regression cycle (Fig. 1c). The lower–middle interval of Member III consists of nodular limestone, thin-bedded argillaceous (dolomitic) limestone, and calcareous mudstone, indicative of deposition in relatively deeper settings, likely below storm wave base (Guo et al., 2013; Mei, 2006). The upper part of Member III contains ‘molar-tooth’ limestone and microbial dolostone with ripple marks, suggesting a brief regression and deposition in a slope to subtidal environment (Mei, 2006). Our samples were collected from the GYZ Formation Member III (Zhangjiayu Member) at four different sections (Gangou, Jixian, Kuancheng, Pingquan, Fig. 1b). In the lower and upper horizons of Member III, two tuff beds yielded U–Pb zircon ages of 1577 ± 12 Ma (Tian et al., 2015) and 1560 ± 5 Ma (Li et al., 2010), respectively.

3. Materials and methods

3.1. Sample preparation method

A total of 223 marine carbonate rocks were selected for this study. Samples were micro-drilled from fresh, unaltered material, avoiding veins, discoloration, and obvious secondary phases, and then ground by hand using an agate pestle and mortar. For bulk carbonate dissolution, $\sim 10\text{--}20$ mg of sample powder ($N = 223$) was dissolved in 5 ml of 2% v/v HNO_3 for 24 h, then centrifuged at 3600 rpm for 5 mins. The supernatant was collected and diluted with 2% v/v HNO_3 for major and trace elemental analysis (e.g., Ca, Mg, Sr, Al, Mn).

For Sr isotope preparation, we followed the newly developed sequential leaching method for argillaceous and dolomitic limestones (Chen and Zhou, 2023), whereby $\sim 50\text{--}100$ mg of micro-drilled sample powder ($N = 133$) is precleaned with 3–5 ml of 1 M ammonium acetate in an ultrasonic bath for 30 mins at room temperature. After centrifugation, the residue was washed once with ultrapure water and centrifuged again. 0.05–0.2 M of acetic acid (HAc), calculated to dissolve $\sim 10\text{--}30\%$ carbonate, was then added to the residue. After the acid was added, samples were ultrasonically agitated for 30 mins and then allowed to stand for another 30 mins at room temperature, before being centrifuged at 3600 rpm for 5 mins. The supernatant was collected for Sr isotope and elemental analysis.

For Li isotope preparation, we followed the leaching method of (Tessier et al., 1979), as tested by many recent studies (Krause et al., 2023; Liu et al., 2022a; Pogge von Strandmann et al., 2019, 2021b), whereby acetic acid was buffered to pH 5 with sodium acetate (NaOAc). 0.75 ml of pH-buffered solution was added to ~ 100 mg of micro-drilled sample powder ($N = 49$), then ultrasonically agitated for 10 mins and left to stand for ~ 5 h at room temperature. The solution was then centrifuged, and the supernatant carefully pipetted out for Li isotope and elemental analysis.

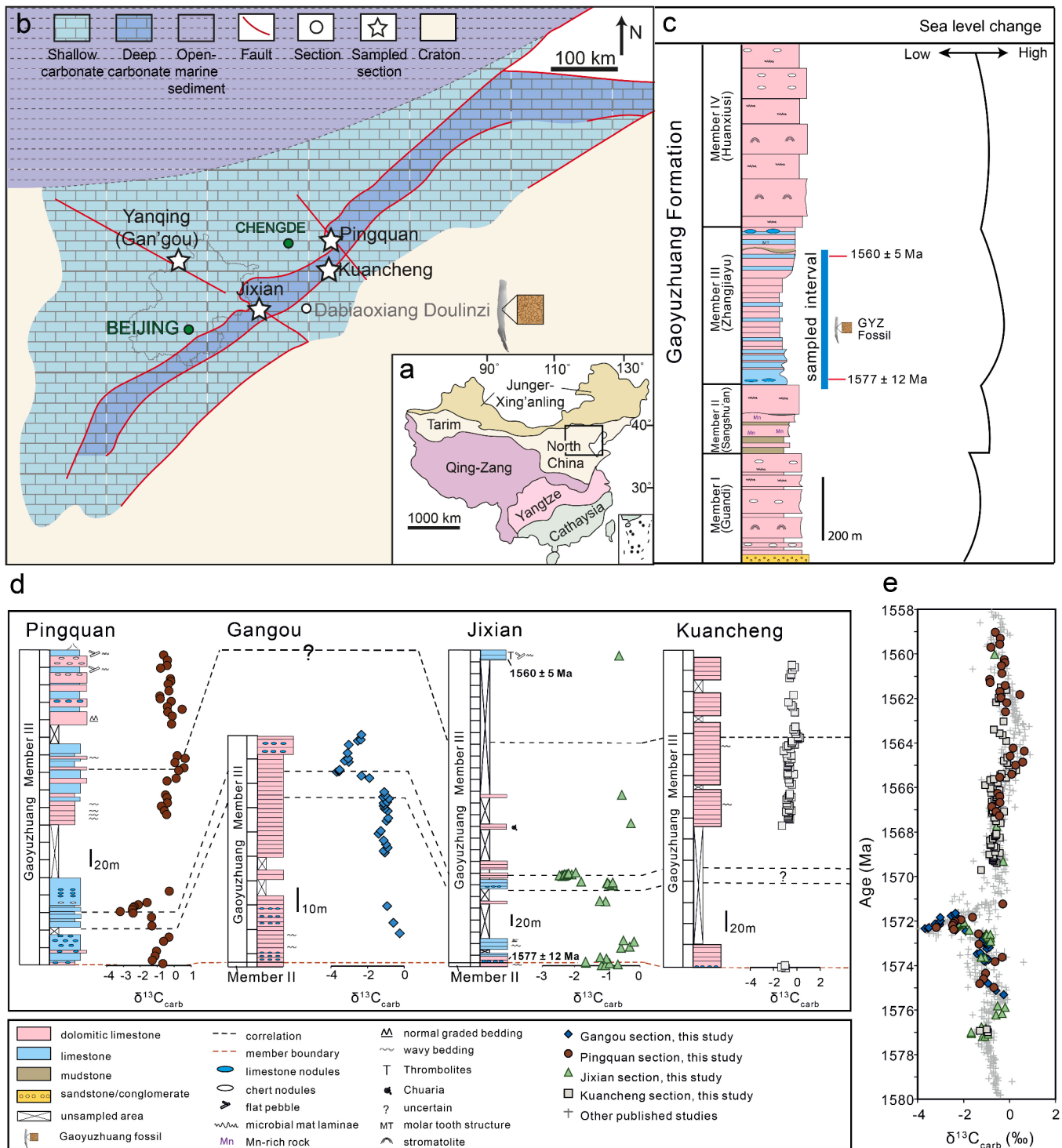


Fig. 1. Geological background of the study area. (a) Major tectonic subdivisions of China, modified after (Shang et al., 2019). The blue box shows the area of panel b (Yanliao Basin, North China). (b) Simplified Mesoproterozoic paleogeographic map of North China during deposition of the Gaoyuzhuang Formation. The four sampling sections are Jixian (40°9'21.77"N, 117°28'39.69"E), Kuancheng (40°36'14.02"N, 118°31'31.75"E), Gangou (40°39'49"N, 116°14'30"E) and Pingquan (40°57'48"N, 118°36'25"E). (c) General stratigraphic columns of Gaoyuzhuang Formation and sea level change (modified from Zhang et al., 2018). (d) Carbon isotope correlation for Gaoyuzhuang Member III across the four sections analysed in this study. (e) Age model for Gaoyuzhuang Member III (and part of Member II) in relation to $\delta^{13}C_{carb}$ data from this study and other published studies (Guo et al., 2013; Shang et al., 2019; Zhang et al., 2018) (shown as grey crosses). Errors are smaller than the symbols used.

3.2. Analytical methods

All geochemical analyses were carried out at the London Geochemistry and Isotope Centre (LOGIC), University College London (UCL). Elemental analyses were performed on solutions of bulk carbonate (2%

v/v HNO₃) and all supernatant leaches prepared for Sr (in HAC) and Li (in NaOAc) isotopes. Major element concentrations in carbonate leachates, including Ca, Mg, Mn, Al and Sr, were measured by inductively coupled plasma optical emission spectrometry (Varian 720 ICP-OES). Each data point represents the average of 6 replicates, with

the RSD being < 3% for all analysed elements. Trace element Rb and Li concentrations of carbonate leachates were analysed by inductively coupled plasma mass spectrometry (Agilent 7900 ICP-MS) with calibration standards (Superco, Sigma-Aldrich) and samples matrix-matched to 50 µg/g Ca (and also to Na content in the case of NaOAc leaches). Each data point represents the average of 7 replicates, with the RSD being < 5% for all the analysed elements.

For Sr isotope analysis, small polypropylene columns with polypropylene frits (~30 µm) and ~1 cm thickness (30–40 mg) of Eichrom® Sr specific resin were used for Sr separation in an ISO 7 (Class 10000) metal-free laboratory with ISO 5 laminar flow hoods at UCL. The supernatant (in 0.05–0.2 M acetic acid) was dried on a hotplate before being dissolved in 0.5 ml of 4 M nitric acid and then passed through the precleaned and conditioned columns. The column was sequentially eluted with 1 ml of 8 M HNO₃, and twice with a full reservoir of 8 M HNO₃ to primarily wash out the matrix. Afterwards, two full reservoirs of Milli-Q water were used to elute Sr. The collected eluant was then dried and redissolved in 2% v/v HNO₃ for conventional ⁸⁷Sr/⁸⁶Sr isotope analysis. The ⁸⁷Sr/⁸⁶Sr isotope ratios were measured using a Nu Instruments Plasma 3 multi-collector inductively coupled plasma mass spectrometer (MC-ICP-MS) at UCL. Instrumental isotopic fractionation (IIF) was corrected using the exponential law (to ⁸⁶Sr/⁸⁸Sr = 0.1194), followed by a standard bracketing method. The interferences of ⁸⁷Rb were corrected using an ⁸⁷Rb/⁸⁵Rb ratio of 0.3857. Interferences for Kr were corrected by a blank measurement before each sample. Reported ⁸⁷Sr/⁸⁶Sr ratios were corrected to the published value of SRM 987 (0.710252 ± 0.000013; Weis et al., 2006). An in-house carbonate standard (N1, modern shell) was processed along with sample leachates and its multi-run average was 0.70918 ± 0.000018 (2 SD, N=10), which is comparable to the modern seawater value (0.709175 ± 0.000012; Kuznetsov et al., 2012). A procedural blank was included in each batch of samples, with Sr quantities of less than 0.01% contribution to sample measurements.

For Li isotope analysis, a two cation-exchange column method was used for Li purification at the LOGIC laboratories (Liu et al., 2022a; Pogge von Strandmann et al., 2019). AG®50 W X-12 resin was used for the cation-exchange procedure and eluted by 0.2 M HCl. Li isotope fractionation during column elution was also monitored by collecting a split of the elution before and after the Li collection, which was then analysed for Li content. All splits had < 0.2% of the total Li, which means the shift in Li isotopes caused by incomplete recovery from columns was less than the long-term precision of the Li isotope ratio measurements (Liu et al., 2022a; Pogge von Strandmann et al., 2021a). Lithium isotopes were measured by a multi-collector ICP-MS (Nu Plasma 3) at UCL. A sample-standard (IRMM-016) bracketing method was applied for Li isotope measurement. A procedural blank was included in each batch of samples with Li quantities of less than 0.03% contribution to the sample measurements. The Li isotope data are reported as the deviation of the ⁷Li/⁶Li ratio in samples from the zero-reference material L-SVEC (⁷Li/⁶Li = 12.17285 ± 0.00023; Magna et al., 2004), which has same isotope ratio as IRMM-016 (Jeffcoate et al., 2004). The reproducibility and accuracy of the Li procedure, including sample digestion, Li separation and Li isotope analysis were checked by repeated measurements of Atlantic seawater ($\delta^7\text{Li} = 31.08\text{‰} \pm 0.48\text{‰}$ relative to L-SVEC, 2 SD, N = 6). Further standards analysed by this method are reported in Pogge von Strandmann et al. (2019).

For C and O isotope analysis, powdered carbonate (N = 192) was analysed at the Bloomsbury Environmental Isotope Facility (BEIF) at UCL on a continuous-flow (ThermoFisher Delta V) mass spectrometer linked to a Gas Bench II device. All values are reported using the Vienna Pee Dee Belemnite notation (VPDB) relative to NBS19. Repeat measurements of the standard NBS 19 gave $\delta^{13}\text{C}_{\text{VPDB}} = 1.95\text{‰} \pm 0.06\text{‰}$ (2 SD, N = 12), $\delta^{18}\text{O}_{\text{VPDB}} = -2.2\text{‰} \pm 0.1\text{‰}$ (2 SD, N = 12).

4. Results and discussion

4.1. Seawater strontium and lithium isotope records

Strontium, Li, C ($\delta^{13}\text{C}_{\text{carb}}$) and O ($\delta^{18}\text{O}_{\text{carb}}$) isotopes, as well as major and trace elements are reported in this study (Fig. 2, Supplementary Data S1) for marine carbonate rocks across four sections of the Gaoyuzhuang Formation (GYZ) Member III. The characteristic negative C isotope excursion of Member III is observed in three sections (Pingquan, Jixian and Gangou; note that its absence in the Kuancheng section reflects lack of exposure), with a robust $\delta^{13}\text{C}_{\text{carb}}$ shift from ~0‰ to ~-4‰ (Fig. 1, 2), with no signs of diagenetic overprinting (see Supplementary Information; Fig. S1). Age models and stratigraphic correlations are constructed based on carbon isotope stratigraphy, cyclostratigraphy, and the published dating constraints (Fig. 1d,e and see Supplementary Information for details). Using the mean U-Pb ages and assuming constant sedimentation rates within each section, we calculate sedimentation rates of ~20–30 m/Myr for the studied interval. These values fall within the typical long-term (~10⁶ yr) accumulation rates (10–100 m/Myr) for carbonate sediments (Schlager, 2010). The resulting ~2 Myr duration of the carbon isotope excursion is consistent with the floating astronomical timescale derived from Milankovitch cycles in Member III of the GYZ Formation at the Jixian and Gangou sections (Liu et al., 2022b).

⁸⁷Sr/⁸⁶Sr and $\delta^7\text{Li}$ in carbonates are sensitive to diagenesis and detrital contamination. To identify samples that best preserve the original seawater signal, we applied a four-step geochemical screening procedure (Fig. S3, S4 and Fig. 3). First, we assessed diagenetic alteration by plotting Mn/Sr, Mg/Ca, and Sr/(Ca+Mg) from bulk carbonate (2% HNO₃) against ⁸⁷Sr/⁸⁶Sr (Fig. S3), using thresholds previously validated for this interval (Mn/Sr < 1–2 g/g, Mg/Ca < 0.05–0.4 g/g, Sr/(Ca+Mg) > 200 µg/g; Chen and Zhou, 2023). Second, we evaluated detrital contamination using Rb/Sr and Al/(Ca+Mg) ratios from Sr leachates against ⁸⁷Sr/⁸⁶Sr (Bellefroid et al., 2018; Chen and Zhou, 2023) and Rb/(Ca+Mg) and Al/(Ca+Mg) ratios from Li leachates against $\delta^7\text{Li}$ (Cao et al., 2022; Pogge von Strandmann et al., 2021a), retaining only samples with low Rb and Al contents (e.g., Rb/Sr < 5 mg/g, Al/(Ca+Mg) < 1 mg/g; Fig. S4). Third, for this screened subset, we tested the robustness of these cutoffs by examining ⁸⁷Sr/⁸⁶Sr and $\delta^7\text{Li}$ against all major alteration indices commonly used for detecting seawater-derived Sr and Li (Mn/Sr, Mg/Ca, Sr/(Ca+Mg), Rb/Sr, Rb/(Ca+Mg), Li/(Ca+Mg), Al/(Ca+Mg), and $\delta^{18}\text{O}$; Fig. 3a). $\delta^7\text{Li}$ values show no correlation with any alteration proxy across the four sections, which suggests that diagenesis and detrital silicate inputs exerted negligible influence on the screened Li isotope record. In contrast, several highly dolomitized Gangou samples exhibit elevated ⁸⁷Sr/⁸⁶Sr ratios that covary with alteration indicators, so only their lowest values that overlap with the least altered samples from the Pingquan, Jixian, and Kuancheng sections were retained. Finally, the screened dataset displays highly consistent ⁸⁷Sr/⁸⁶Sr and $\delta^7\text{Li}$ values across different sections, yielding identical stratigraphic trends regardless of mineralogy (limestone versus dolomitic limestone; Fig. 3b), and falling within the range of the globally least altered Mesoproterozoic carbonates (Chen et al., 2022b; Kalderon-Asael et al., 2021).

Member III of the GYZ Formation records deposition during a transgressive maximum, spanning environments from below storm wave base (during the excursion) to slope and deeper subtidal settings (above the excursion), where seawater was likely well mixed and only minimally influenced by meteoric input, lagoonal processes, or restricted circulation (Luo et al., 2025). Stratigraphic sections distributed along a lateral gradient from relatively deeper-water settings (Jixian, Pingquan) to shallower-water settings (Gangou) show identical $\delta^{13}\text{C}$, ⁸⁷Sr/⁸⁶Sr, and $\delta^7\text{Li}$ excursions. This agreement demonstrates that the isotope signals are not facies controlled. When combined with petrographic observations (Fig. S2) and multi-step alteration assessments, the convergence of isotope profiles across sections strongly support that the screened data

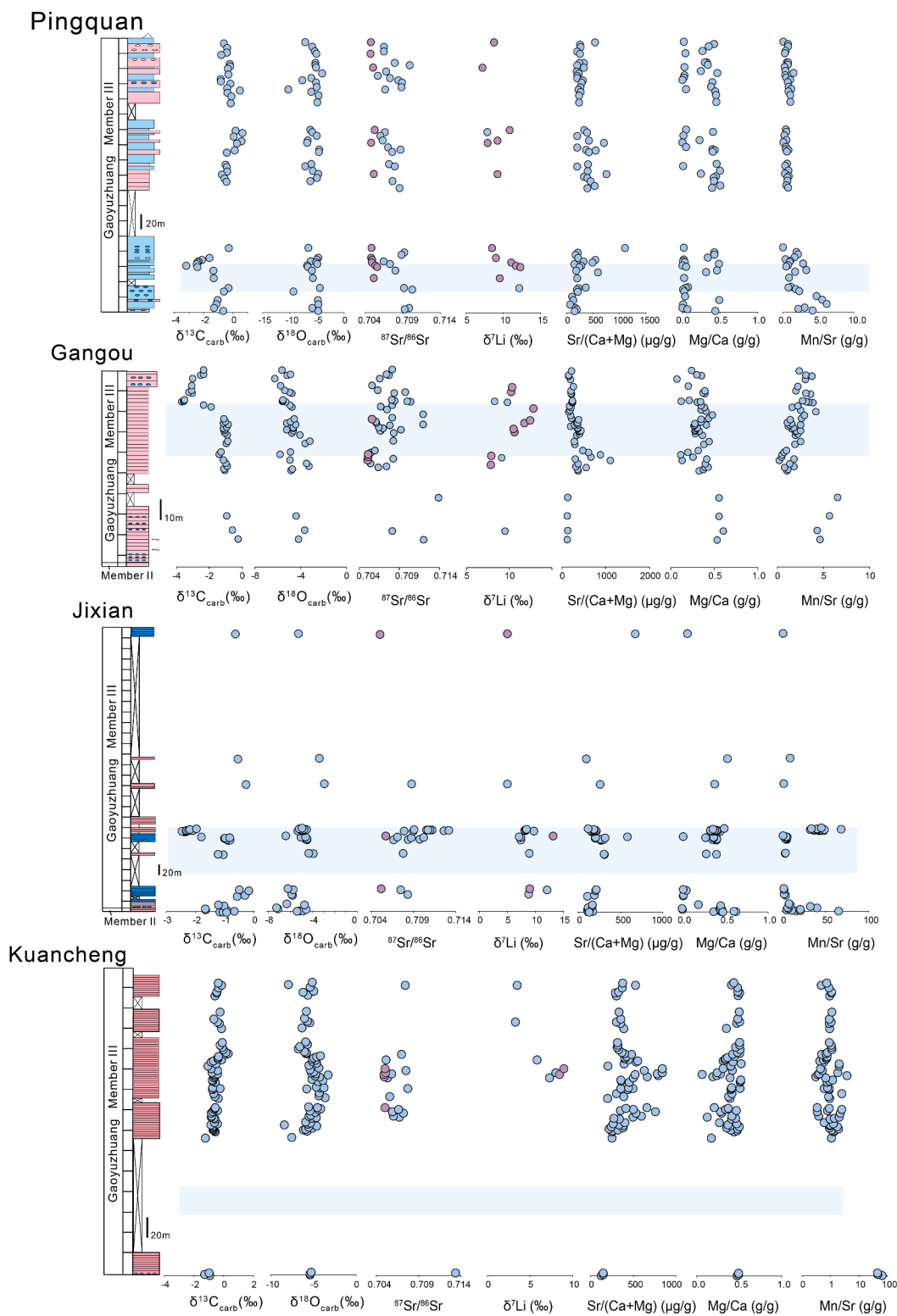


Fig. 2. Geochemical profiles for individual stratigraphic sections through Member III of the Gaoyuzhuang Formation. Carbonate $\delta^{13}\text{C}$, $\delta^{18}\text{O}$, $^{87}\text{Sr}/^{86}\text{Sr}$, and $\delta^7\text{Li}$, together with bulk carbonate $\text{Sr}/(\text{Ca}+\text{Mg})$, Mg/Ca , and Mn/Sr for the four measured sections are shown here. All data are from this study and are plotted against stratigraphic height. Mn/Sr values for the Jixian and Kuancheng sections are shown on a logarithmic scale. The blue interval marks the carbon isotope excursion. Purple symbols in the Sr and Li profiles indicate samples that passed the geochemical screening and are interpreted to best preserve original seawater signals. Because the trends of the screened Sr and Li isotopes, particularly for Sr, are difficult to resolve at this scale, detailed trends can be seen in [Figures 3 and 4](#). Reported $\delta^7\text{Li}$ values represent carbonate Li isotope compositions and are not corrected for carbonate–seawater fractionation. The full dataset and additional elemental data are provided in the Supplementary Material.

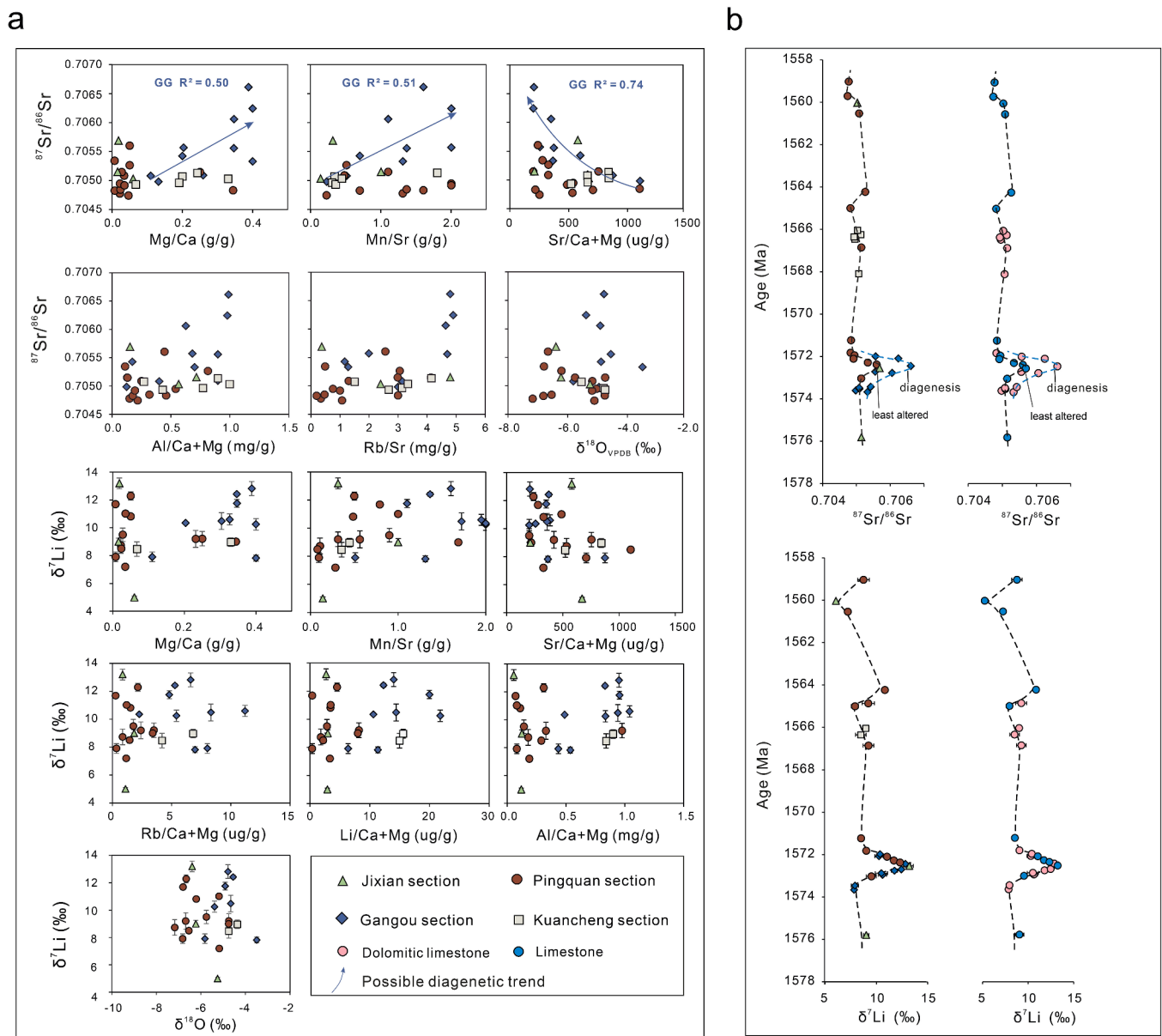


Fig. 3. Screening procedure Step 3 and Step 4 – evaluation of cutoff validity. a) Step 3: Plots of $^{87}\text{Sr}/^{86}\text{Sr}$ and $\delta^7\text{Li}$ values for samples that passed the Step 1 and Step 2 screening plotted against indicators of diagenesis and detrital contamination. Only trendlines with $R^2 \geq 0.5$ are shown. Apart from elevated $^{87}\text{Sr}/^{86}\text{Sr}$ ratios in the Gangou (GG) section, the $^{87}\text{Sr}/^{86}\text{Sr}$ ratios in the other three sections and all $\delta^7\text{Li}$ values show no evidence of alteration. Mg/Ca, Mn/Sr, and Sr/(Ca+Mg) ratios were measured in bulk carbonate dissolved in 2% HNO₃. For Sr isotope plots, Rb/Sr and Al/(Ca+Mg) were measured in Sr leachates obtained using acetic acid. For Li isotope plots, Al/(Ca+Mg), Rb/(Ca+Mg), and Li/(Ca+Mg) were measured in Li leachates obtained using sodium acetate. b) Step 4: Inter-section comparison. Sr and Li isotope data for samples that passed the Step 1 and Step 2 criteria are shown by stratigraphic position and Mg/Ca ratios. The black line indicates the trend defined by least altered samples. The blue line highlights diagenetically altered samples with higher $^{87}\text{Sr}/^{86}\text{Sr}$ values from dolomitic limestones in the Gangou section, consistent with alteration patterns observed in panel (a). Error bars for $\delta^7\text{Li}$ represent two standard deviations (N = 3); other analytical uncertainties are smaller than the symbol size.

captured a genuine global seawater perturbation rather than diagenetic overprinting or localized restricted-basin effects. For details of sample screening at each step, see the **Supplementary Information**.

Seawater $\delta^7\text{Li}$ values were then estimated from measured rock values by the addition of 5‰ on average (full range 3–8.5‰) (Day et al., 2021; Krause et al., 2023; Marriott et al., 2004; Pogge von Strandmann et al., 2013; Pogge von Strandmann et al., 2019), to correct for isotopic fractionation during Li incorporation into carbonates (see **Supplementary Information**). The seawater $^{87}\text{Sr}/^{86}\text{Sr}$ and $\delta^7\text{Li}$ values for the three sections that document the C isotope excursion show a coupled increasing trend towards the nadir of the $\delta^{13}\text{C}_{\text{carb}}$ excursion (-4‰), with a Sr isotope increase from ~ 0.7050 to ~ 0.7057 and a Li isotope increase

from $\sim 13\text{‰}$ to $\sim 18\text{‰}$ (Fig. 4). After reaching peak values, Sr isotope ratios decrease to ~ 0.7048 , before returning to ~ 0.7050 , while Li isotope values return to $\sim 13\text{‰}$ and remain around this level. $\delta^{13}\text{C}_{\text{carb}}$ values likewise recover to a consistent value of $\sim 0\text{‰}$ (Fig. 4).

4.2. Modelling the Sr and Li positive isotope excursion

Dynamic Sr and Li isotope box models have been developed by previous studies (Nana Yobo et al., 2021; Pogge von Strandmann et al., 2013; Pogge von Strandmann et al., 2021b), and are used here to constrain which of the key potential factors (including the hydrothermal flux, river input flux and its isotope composition, and marine reverse

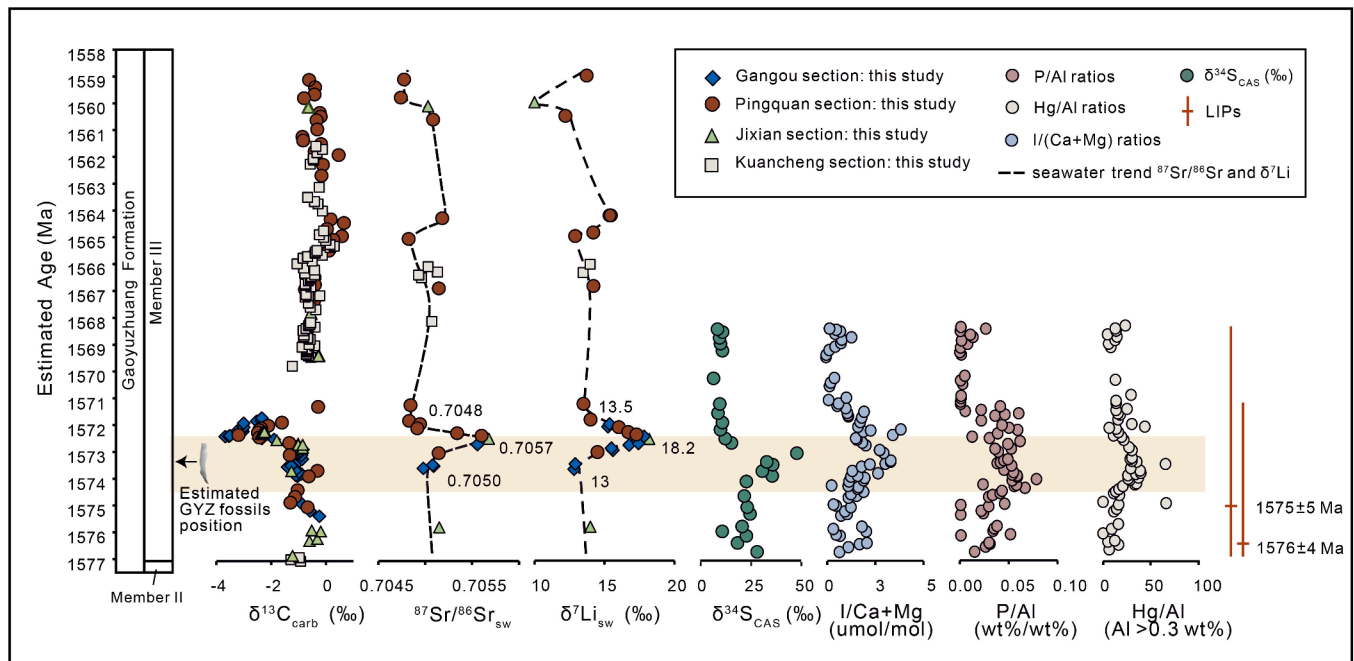


Fig. 4. Integrated geochemical profiles through Gaoyuzhuang Formation Member III. C, Sr and Li isotopes are from the four sections (Gangou, Jixian, Pingquan, Kuancheng) of this study. An average fractionation factor (5‰) has been applied to the $\delta^7\text{Li}$ profile to estimate seawater values (see Supplementary Information for details). A coupled positive excursion in seawater Sr and Li isotopes correlates to the negative C isotope excursion (shown by the yellow band). $\delta^{34}\text{S}_{\text{CAS}}$, I/(Ca + Mg), P/Al and Hg/Al are from published studies of the Gangou section (Shang et al., 2019; Tang et al., 2022; Xie et al., 2023). Intensified volcanic activity is evidenced by large igneous provinces (LIPs), such as in Amazonia (1576 ± 4 Ma; Teixeira et al., 2019) and West Africa (1575 ± 5 Ma; Teixeira et al., 2019). Slight differences in the starting points of $\delta^{34}\text{S}_{\text{CAS}}$, I/(Ca + Mg), P/Al, and Hg/Al (from other studies) compared to Sr and Li isotopes (this study) may result from uncertainties in stratigraphic correlation. Analytical uncertainties are smaller than the size of the symbols.

weathering) are the likely controls on the observed covariation in Li and Sr isotopes. The model begins with an initial steady state in which input and output fluxes are balanced. To reflect higher Precambrian ridge-spreading and outgassing rates (e.g., Tajika and Matsui, 1992), the modern hydrothermal flux (F_h) for both Sr and Li were doubled (Kalderon-Asael et al., 2021). Riverine fluxes (F_r) were then adjusted to reproduce the measured pre-excursion seawater values. To account for radiogenic evolution, riverine (R_r) and hydrothermal (R_h) $^{87}\text{Sr}/^{86}\text{Sr}$ ratios were taken from contemporaneous river and mantle evolution curves (Shields, 2007; Workman and Hart, 2005), while the diagenetic reflux (R_{diag}) was set equal to coeval seawater (Richter and Liang, 1993). For lithium isotopes, riverine input ($R_r = 5.8\%$) follows modelled Precambrian values (Kalderon-Asael et al., 2021), consistent with reduced isotope fractionation during clay formation under warmer conditions (Li and West, 2014). Hydrothermal Li isotope compositions were assumed to be similar to modern systems (Coogan and Dosso, 2012). A reduced Li isotope fractionation between seawater and authigenic clays ($\Delta^7\text{Li} = 7\%$; Kalderon-Asael et al., 2021), compared with the modern ocean (16‰; Misra and Froelich, 2012), was used to reflect enhanced Precambrian reverse weathering (Isson and Planavsky, 2018; Kalderon-Asael et al., 2021; Krissansen-Totton and Catling, 2020). The resulting initial residence times for both seawater Sr and Li are close to the modern values (Basu et al., 2001; Kalderon-Asael et al., 2021). Our model for seawater Sr and Li isotopes is solved in 10 kyr steps. The model structure and input parameters are detailed in the **Supplementary Information** and **Table S1**.

Based on the age model, $\delta^7\text{Li}$ (from $\sim 13\%$ to $\sim 18\%$) and $^{87}\text{Sr}/^{86}\text{Sr}$ (from ~ 0.705 to 0.7057) increased to peak values within ~ 1 Myr (Fig. 4). We first used the Sr isotope system, which is highly sensitive to hydrothermal input (Pogge von Strandmann et al., 2013), to explore whether changes in hydrothermal flux alone could drive the excursion. A ≥ 10 -fold decrease in hydrothermal flux would be required to reproduce the Sr isotope peak. Such a decrease is geologically implausible,

particularly during periods of supercontinent breakup when hydrothermal activity is generally expected to increase. Even this extreme scenario, however, could produce only a $\sim 2\%$ increase in $\delta^7\text{Li}$ (Fig. S5a). Thus, hydrothermal changes alone cannot explain the observations. Increasing the weathering flux would lead to an increase in seawater $^{87}\text{Sr}/^{86}\text{Sr}$, as river input is more radiogenic than seawater in our model (Supplementary Information). However, since the riverine input $\delta^7\text{Li}$ is lower than that of seawater (due to marine clay minerals preferentially incorporating ^6Li), this increased weathering flux would lead to a decrease, rather than an increase, in seawater $\delta^7\text{Li}$ (Fig. S5b). Simultaneous increases in riverine Sr and Li isotope ratios without changing fluxes would require a rise of $\sim 14.5\%$ in riverine $\delta^7\text{Li}$ and ~ 0.0035 in riverine $^{87}\text{Sr}/^{86}\text{Sr}$ to achieve the observed peak values (Fig. S5c). Such a substantial increase (~ 0.0035) in the riverine Sr isotope ratio, however, appears improbable, as it surpasses both the magnitude of the shift in riverine $^{87}\text{Sr}/^{86}\text{Sr}$ ratios resulting from Himalayan erosion and weathering over the last 40 Myr (Richter et al., 1992), and the net impact of the highly radiogenic Ganges-Brahmaputra system on the contemporary oceanic Sr budget (Richter and Turekian, 1993).

Therefore, changing hydrothermal flux, river flux, or riverine isotope composition in isolation cannot reproduce the coupled Sr and Li excursions; combination of flux and isotope changes is required. In all combined scenarios we tested (Fig. S6 and Supplementary Information), we were unable to match the observed Sr and Li isotope trends when the weathering flux and riverine $\delta^7\text{Li}$ were held constant, regardless of adjustments to hydrothermal flux or riverine $^{87}\text{Sr}/^{86}\text{Sr}$. Our results show that both an increase in continental weathering flux and an increase in riverine $\delta^7\text{Li}$ input are consistently required, whereas riverine $^{87}\text{Sr}/^{86}\text{Sr}$ and hydrothermal flux may vary depending on the magnitude of weathering change. For example, a smaller increase in weathering flux could be partly offset by a larger rise in riverine $^{87}\text{Sr}/^{86}\text{Sr}$ or a reduction in hydrothermal input, and vice versa. Given the high uncertainties associated with changes in Precambrian riverine $^{87}\text{Sr}/^{86}\text{Sr}$

and hydrothermal flux, and since neither factor can dominate or independently drive the observed Sr and Li peaks, we present here the simplest admissible scenario (Fig. 5), in which both riverine Sr isotope composition and hydrothermal flux are held constant during the rising limb of the excursion. Using the Sr isotope system to constrain the required weathering increase, and then applying this constraint to the Li isotope model, yields a 2.8-fold increase in continental weathering flux together with an approximately 12‰ (range 10–13‰) rise in riverine $\delta^7\text{Li}$ (Fig. 5). It is important to note that although absolute values of weathering flux and riverine $\delta^7\text{Li}$ may vary when riverine $^{87}\text{Sr}/^{86}\text{Sr}$ and hydrothermal flux are allowed to change, the required direction of change (higher weathering flux and higher riverine $\delta^7\text{Li}$) is consistent across all viable model configurations that reproduce the observed seawater Sr and Li peaks (Fig. S6 and Supplementary Information). Consequently, the inferred shift in the weathering regime, as defined by the direction of change in both weathering flux and riverine $\delta^7\text{Li}$ (discussed in the following section), remains robust despite uncertainties in individual model parameters.

Another possibility to explain seawater Li isotope variability concerns an increase in the fractionation factor ($\Delta\text{Li}_{\text{sw-sink}}$) during marine reverse weathering. Given the increased riverine flux (2.8 times) constraint from Sr isotopes, an increase in $\Delta\text{Li}_{\text{sw-sink}}$ to 21‰ would be required to explain the coeval Li isotope excursion (Fig. S5d). This value

is even higher than the modern value ($\sim 16\text{‰}$) (Misra and Froelich, 2012), which seems unlikely, as the biologically controlled Si cycle that dominates today was absent in the Precambrian, and there was no known evidence for widespread chert deposition during the study interval (Krissansen-Totton and Catling, 2020). Instead, studies suggest that the Precambrian ocean experienced intensified reverse weathering, driven primarily by silica oversaturation and potentially enhanced by elevated concentrations of Fe and other clay-forming ions in ferruginous deep waters (Isson and Planavsky, 2018; Kalderon-Asael et al., 2021; Krissansen-Totton and Catling, 2020; Poulton and Canfield, 2011). Such conditions would tend to lower, rather than increase the Li isotope fractionation factor. Other effects, such as temperature and pH changes, are also unlikely to have driven the observed Li isotope shifts (see Supplementary Information). Therefore, the scenario of increased continental weathering coupled with increased river $\delta^7\text{Li}$ remains the most plausible explanation for the coupled positive Sr-Li isotope excursion at ~ 1.57 Ga.

After reaching peak values, $\delta^7\text{Li}$ returned to its initial value, while $^{87}\text{Sr}/^{86}\text{Sr}$ declined to a lower than initial value (0.70484), within ~ 1.2 Myr. The observed recovery trend cannot be fully explained by scenarios such as solely decreasing riverine input values or altering the weathering flux (Supplementary Information and Fig. S7). Given modern oceanic residence times, a twofold increase in hydrothermal input is

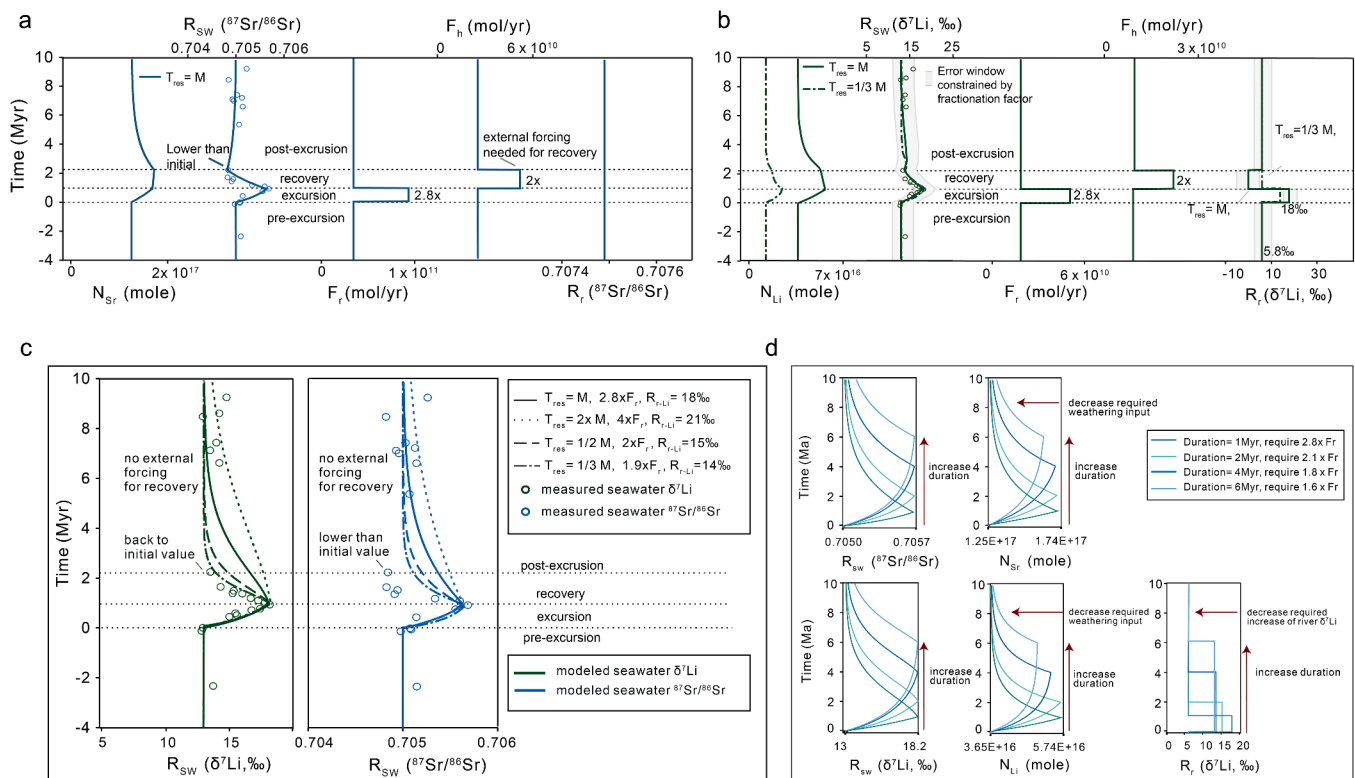


Fig. 5. The simplest successful modelling scenario for reproducing the observed seawater Sr and Li isotope excursions, sensitivity tests for residence time and excursion duration. **a)** Model results for seawater Sr isotopes. In the simplest scenario that assumes modern residence time and unchanged riverine Sr isotope composition, the observed increase in $^{87}\text{Sr}/^{86}\text{Sr}$ requires a 2.8 times increase in continental weathering flux (F_{r}), while the recovery requires a two times increase in hydrothermal input (F_{h}). **b)** Model results for seawater Li isotopes. The timing of changes in F_{r} and F_{h} is constrained by the Sr isotope model under modern residence time. The shaded band represents the uncertainty window defined by the full range of published fractionation factors for Li incorporation into carbonates (3 to 8.5‰; Day et al., 2021; Krause et al., 2023; Marriott et al., 2004; Pogge von Strandmann et al., 2013; Pogge von Strandmann et al., 2019). Under modern residence time, reproducing the observed excursion requires an increase in riverine $\delta^7\text{Li}$ of approximately 12‰ (range 10 to 13‰) during the rising limb and a decrease to $\sim 0\text{‰}$ during the recovery. A reduced residence time (1/3 modern) requires a smaller increase in riverine $\delta^7\text{Li}$ to reach the peak and yields rapid recovery without further lowering of riverine $\delta^7\text{Li}$ (green dash line). **c)** Sensitivity to residence time. Shorter oceanic residence times reduce the magnitude of the required increase in continental weathering flux (F_{r}) and riverine $\delta^7\text{Li}$ (R_{r}), and allow a more rapid recovery of seawater isotopes. Reducing the Li residence time to one third of the modern value permits Li to recover to its initial composition without any additional decrease in riverine $\delta^7\text{Li}$, although this does not apply to Sr isotopes. **d)** Sensitivity to excursion duration for the rising limb. Increasing the duration of the rising limb from 1 to 4 million years reduces the required increase in weathering flux from 2.7 to 1.8 times, and lowers the required riverine $\delta^7\text{Li}$ shift from 18‰ to 14‰. T_{res} = residence time; M = modern residence time; N = seawater reservoir size; R = isotopic ratio; F = flux; sw = seawater; r = river; h = hydrothermal. Symbols are larger than analytical uncertainties.

necessary to account for the decreasing trend in $^{87}\text{Sr}/^{86}\text{Sr}$ ratios (Fig. 5a). However, this change alone cannot restore seawater $\delta^7\text{Li}$ to its initial value, as marine $^{87}\text{Sr}/^{86}\text{Sr}$ is considerably more sensitive to hydrothermal input than $\delta^7\text{Li}$ (Pogge von Strandmann et al., 2013). An additional decrease in riverine $\delta^7\text{Li}$ to zero or a negative value would be required to match the observed trend (Fig. 5b, solid line). Such a decrease, however, is less realistic as it would imply riverine $\delta^7\text{Li}$ values lower than the average for primary silicate rocks (Pogge von Strandmann et al., 2021a). A sensitivity test on the residence time shows that reducing the oceanic residence times of Sr and Li leads to a rapid recovery and lowers the magnitude of change required in both weathering flux and riverine $\delta^7\text{Li}$ to reproduce the observed peak values (Fig. 5c). A shortened Li residence time is plausible, as enhanced marine reverse weathering during the Precambrian would have reduced the seawater Li inventory. With the residence time reduced to 1/3 of modern, Li isotopes can recover within ~ 1 Myr without additional forcing (Fig. 5c). This is not applicable for Sr isotopes, and an external forcing is necessary to achieve lower $^{87}\text{Sr}/^{86}\text{Sr}$ ratios during the recovery phase relative to the initial values (Fig. 5c). Within the framework of partial breakup of the supercontinent Nuna (Lu et al., 2002), and excluding other potential scenarios, the recovery of Sr and Li isotope ratios might reasonably be attributed to an increased hydrothermal input, with the reduced residence time for the Li reservoir (Fig. 5a, 5b). Details of failed recovery scenarios are provided in the **Supplementary Information**.

A sensitivity test on duration (Fig. 5d) shows that lengthening the rising limb of the excursion from 1 to 4 Myr reduces the required increase in weathering flux from 2.7 to 1.8 times and lowers the required riverine $\delta^7\text{Li}$ from 18‰ to 14‰. The total duration of ~ 2 Myr (including both the rise and recovery) adopted in our box modelling likely represents a minimum estimate, as independent constraints from the Sr isotope system indicate that a substantially shorter excursion is unlikely (**Supplementary Information**). Our residence time and duration tests demonstrate that the observed Sr and Li isotope excursion is geochemically feasible across a reasonable parameter space, but improved geochronology will further refine this framework. Additional sensitivity tests addressing uncertainties in the age model, hydrothermal flux, and fractionation factor are provided in the **Supplementary Information (Figs. S8-S10)**.

4.3. Changes in weathering regime and its possible driving mechanisms

In modern settings, riverine (dissolved) $\delta^7\text{Li}$ plotted against weathering intensity shows a “boomerang” shape, whereby the highest riverine $\delta^7\text{Li}$ corresponds to a moderate weathering intensity with increased clay formation (incongruent weathering; Dellinger et al., 2015; Pogge von Strandmann et al., 2021b), while the dissolved Li yield (weathering flux) decreases towards the high-intensity regime (Pogge von Strandmann et al., 2021b). Our modelling results indicate that the increasing trend observed for the Sr-Li isotope excursion is primarily driven by an enhanced continental weathering flux, coupled with elevated riverine $\delta^7\text{Li}$. This model result aligns with a weathering regime shift from high intensity (transport-limited and congruent weathering) towards moderate intensity (higher denudation rates and incongruent weathering).

A decrease in weathering intensity with an increased weathering flux may have been driven either by warming episodes (increase in CO_2 degassing; Krause et al., 2023; Pogge von Strandmann et al., 2013) or by increased tectonic uplift with more fresh rocks being exposed and weathered (Caves Rugenstein et al., 2019; Misra and Froelich, 2012). Although tectonic uplift seems unlikely to fit an event of such short duration, the influence of orogenic activity cannot be fully dismissed. The final stages of Nuna assembly likely occurred ~ 1.6 Ga (Pourteau et al., 2018) through the collision between north Australia and Laurentia, and palaeocontinental reconstruction suggests that the North China Craton was then connected to the North Australia Craton (Zhang et al., 2012). The estimated high $p\text{CO}_2$ levels across the study interval

(Zhang et al., 2022) suggest the presence of an external carbon source to offset carbon consumption by higher weathering rates. CO_2 degassing from intensive volcanism during this period is supported by Hg enrichment and mercury isotope anomalies in marine sediments (Luo et al., 2024; Tang et al., 2022; Yang et al., 2025), the emplacement of large igneous provinces (Baratoux et al., 2019; Teixeira et al., 2019), and a potentially global plume event (Condie et al., 2023), occurring across and preceding the excursion (Fig. 4). Increased $p\text{CO}_2$ would have enhanced global surface temperatures, leading to an intensified hydrological cycle and increased rainfall (Krause et al., 2023). In the meantime, the orogenic activity and volcanic eruptions may have supplied more weatherable fresh rock surfaces. As a result, the denudation rate (D) would have increased (Pogge von Strandmann et al., 2021b), leading to enhanced clay mineral formation, resulting in increased incongruent weathering and elevated riverine $\delta^7\text{Li}$ values. An analogous silicate weathering scenario has been observed in the Cenozoic Era (Krause et al., 2023), when increased clay formation sequestered carbonate-forming cations, thus playing a key role in sustaining the Middle Eocene Climatic Optimum. This scenario also aligns well with the sustained high $p\text{CO}_2$ levels and warm climate during the study period. The integration of our data, geological evidence and modelling outcomes therefore supports the hypothesis of a volcanism-induced weathering event affecting tectonically uplifted terrains, triggering an increase in continental weathering rates and a decrease in weathering congruency.

4.4. Links to the Mesoproterozoic carbon cycle and ocean oxygenation

Seawater $^{87}\text{Sr}/^{86}\text{Sr}$ and $\delta^7\text{Li}$ values initially increased prior to the negative CIE, but their peak and falling limb coincide with the nadir and recovery of $\delta^{13}\text{C}_{\text{carb}}$, respectively (Fig. 4). An increase in the isotopic composition of carbonate-associated sulfate ($\delta^{34}\text{S}_{\text{CAS}}$) occurs almost coincident with increasing seawater Sr and Li isotopes, followed by a sharp decline below the CIE (Xie et al., 2023), while positive I/(Ca+Mg) and P/Al excursions (Shang et al., 2019) occur prior to and across the CIE (Fig. 4). Slight offsets between the initial rises in I/(Ca+Mg) and P/Al reported in previous studies (Shang et al., 2019) and the timing of the Sr and Li isotope excursions likely reflect uncertainties in stratigraphic correlation or differences in proxy residence times. Iodine and phosphorus have oceanic residence times that are several orders of magnitude shorter than those of Sr and Li (Broecker and Peng, 1983), and therefore respond rapidly to local redox or environmental changes, whereas Sr and Li record more slowly integrated global weathering signals. Multiple studies based on independent redox proxies (e.g., $\delta^{53}\text{Cr}$, $\delta^{98}\text{Mo}$, I/(Ca+Mg) ratios, $\delta^{34}\text{S}_{\text{CAS}}$, Ce anomalies) have suggested that the negative carbon isotope excursion in GYZ Member III most likely resulted from an oceanic oxygenation event (Luo et al., 2020, 2025; Shang et al., 2019; Tang et al., 2022; Xie et al., 2023; Xu et al., 2023; Zhang et al., 2018). Based on these observations, we propose a plausible connection between the changes in the weathering regime and the associated carbon cycle perturbations, ocean oxygenation, and biological evolution that occurred during deposition of the GYZ Formation.

Initially, the weathering regime was transport-limited, characterised by low $\delta^7\text{Li}$ and $^{87}\text{Sr}/^{86}\text{Sr}$ ratios (as discussed above), with low riverine sulfate and nutrient inputs (Guo et al., 2015; Xie et al., 2023) (Fig. 4, 6a). The pulse of volcanism (Luo et al., 2024; Tang et al., 2022; Yang et al., 2025) intensified volcanic CO_2 degassing, triggered greater continental weathering and increased in the sulfate influx to the oceans. Given the low seawater sulfate concentrations envisaged for this interval (Guo et al., 2015; Xie et al., 2023), an initial increase in nutrient inputs through weathering led to sulfate-limited pyrite burial, potentially combined with greater isotopic fractionation during microbial sulfate reduction (Habicht et al., 2002), resulting in a positive shift in measured $\delta^{34}\text{S}_{\text{CAS}}$ (Xie et al., 2023). Continued weathering, indicated by Sr and Li isotope peaks, may then have triggered a pulse of sulfate into the ocean, thus overturning the effects of pyrite burial on seawater $\delta^{34}\text{S}$ due to a

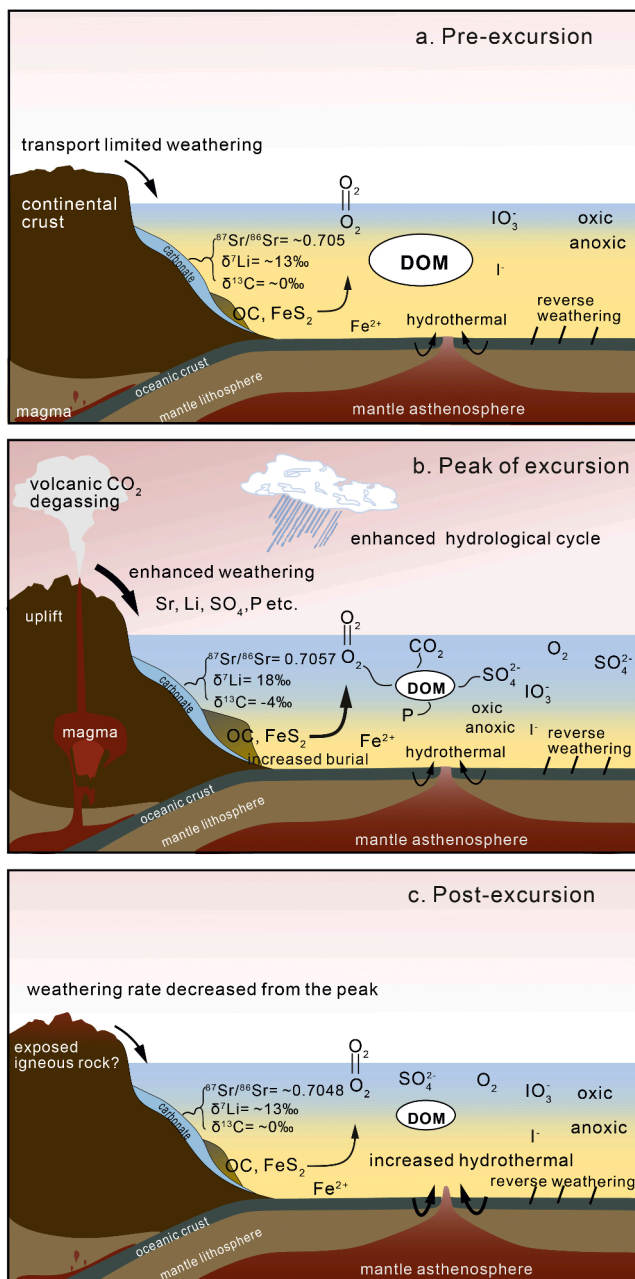


Fig. 6. Conceptual model linking the weathering event to carbon cycle perturbation and marine oxygenation. The arrow width represents the relative magnitude of each flux. **a)** Prior to the Sr and Li isotope excursion. The general Mesoproterozoic climate was warm, and weathering regime was transport-limited, accompanied by low sulfate and nutrient inputs, with a prominent level of oceanic anoxia. **b)** The peak of the Sr and Li isotope excursion. Increased volcanic degassing, coupled with accretional orogenic uplift, triggered an enhanced weathering rate with more secondary mineral formation (incongruent weathering), resulting in an increase in seawater Sr and Li isotope values. Elevated sulfate and nutrient inputs led to enhanced productivity and pyrite burial, potentially raising oxygen levels. The increased availability of marine oxidants (O_2 and SO_4) oxidized dissolved organic matter (DOM) and drove the carbon isotope excursion. DOM oxidation likely further released CO_2 and P, sustaining the weathering. **c)** After the Sr and Li isotope excursion. Cessation of DOM oxidation and reduced weathering gradually returned Sr, Li and C isotope values to their initial state, and prompted a return of widespread oceanic anoxia. The lower Sr isotope value compared to the initial state may potentially be attributed to an increased hydrothermal flux, possibly in conjunction with greater exposure of relatively unradiogenic igneous rock.

combination of a lower proportion of pyrite burial relative to the sulfate input, and a greater flux of isotopically lighter riverine sulfate (Shields et al., 2019) (Fig. 4, 6b). Elevated phosphorus influx (Shang et al., 2019; Fig. 4) and higher carbonate-associated phosphate (Xie et al., 2024), together with increased bioessential micronutrients' input such as Cu, Zn, and Ni (Luo et al., 2024), point to enhanced continental nutrient supply during this interval. Increased nutrient supply would have stimulated primary productivity and organic carbon burial (Fig. 6b), as evidenced by heavier $\delta^{66}\text{Zn}$ values during the study interval, interpreted to reflect the preferential burial of isotopically light Zn with organic matter and the enrichment of residual seawater in heavy Zn (Song et al., 2024). Elevated TOC contents in coeval strata provide additional support for increased organic carbon burial (Zhang et al., 2018). In contrast, the muted $\delta^{138}\text{Ba}$ response likely reflects buffering in a low-sulfate Mesoproterozoic ocean, in which limited barite precipitation allowed dissolved Ba to accumulate and reduced the sensitivity of Ba isotopes to productivity-driven changes (Li et al., 2025).

Although increased organic carbon burial is typically associated with a positive CIE, the Proterozoic carbon isotope record has been proposed to be insensitive to such changes due to counterbalancing effects from the weathering of isotopically light organic carbon (Daines et al., 2017). Increased sulfate weathering associated with pyrite burial may have acted as an additional oxygen source (Shields et al., 2019), as evidenced by the positive $\delta^{34}\text{S}_{\text{CAS}}$ isotope excursion (Fig. 4, 6b). Changes in ocean redox conditions and oxygenation are evidenced by elevated $\text{I}/(\text{Ca}+\text{Mg})$ ratios in carbonates (Shang et al., 2019; Fig. 4, 6b), which reflect increased iodate (IO_3^-) in more oxic waters, as iodate is the only iodine species that can be incorporated into carbonate minerals (Lu et al., 2010). The ocean oxygenation is further corroborated by independent redox proxies in the same interval, including negative Ce anomalies (Chen et al., 2025; Zhang et al., 2018), enrichment in ferric (oxyhydr) oxide minerals (Zhang et al., 2018) and a positive Mo isotope excursion (Xu et al., 2023). The increased availability of oxidants in the ocean, such as sulfate and oxygen, likely led to enhanced remineralization (oxidation) of marine organic matter, causing the $\delta^{13}\text{C}_{\text{carb}}$ composition of marine dissolved inorganic carbon to decrease (Chen et al., 2022a; Rothman et al., 2003; Shi et al., 2022). The release of organically bound P and C through the oxidation of DOM would likely have resulted in elevated oceanic P and atmospheric CO_2 levels (Alcott et al., 2022; Dodd et al., 2023). The increased $p\text{CO}_2$ would then have sustained or further accelerated silicate weathering and P input to the ocean, which may explain the peaks in P and Sr-Li isotopes observed across the negative CIE (Fig. 4, Fig. 6b). As the available oxidant (e.g., O_2 , SO_4) in the ocean was more limiting than during later times in Earth history, ocean oxidation could not be sustained and $\delta^{13}\text{C}_{\text{carb}}$ values returned to their initial levels (Fig. 6c). Cessation of surplus marine organic matter remineralisation and reduced continental weathering would then have reduced the P input to the ocean, thus causing a decrease in organic carbon and pyrite burial, as well as a return to more widespread anoxia (Fig. 6c).

Beyond marine oxygenation, several studies have also proposed a rise in atmospheric oxygen during this interval. For example, positive Cr-isotope values have been interpreted to mark the onset of oxic Cr cycling at atmospheric $p\text{O}_2$ levels greater than approximately 0.1–1% PAL (Xie et al., 2023). However, other work shows that Cr-isotope fractionation can arise independently of atmospheric oxygen through non-redox processes, localized Cr cycling, or diagenetic modification, limiting its reliability as a quantitative proxy for atmospheric $p\text{O}_2$ (Oze et al., 2016; Saad et al., 2017; Wang et al., 2021). Mass-balance calculations using Mo isotopes and estimates from $\text{I}/(\text{Ca}+\text{Mg})$ have been extrapolated to suggest that widespread ocean oxygenation during the studied interval may have required atmospheric oxygen levels exceeding roughly 4% PAL; however, translating marine redox proxies into atmospheric conditions necessarily involves assumptions and uncertainties (Shang et al., 2019; Xu et al., 2023). Although such estimates imply that oxygen could have crossed thresholds considered necessary

for early eukaryotic respiration (>0.1–1% PAL; Runnegar, 1991; Sperling et al., 2013), microbiological and evolutionary studies emphasize that eukaryogenesis required multiple biological and ecological innovations and was not governed by oxygen availability alone (Butterfield, 2009, 2015; Porter, 2020). The relationship between Mesoproterozoic oxygen dynamics and early eukaryotic evolution remains complex and requires further investigation. Despite these uncertainties, the Mesoproterozoic is increasingly recognised as a dynamic interval marked by episodic oxygenation that may have deepened the redox chemocline and expanded oxic habitats (Luo et al., 2025). The oxygenation event documented here coincides with the appearance of unusually large GYZ macrofossils (up to 30 cm; Zhu et al., 2016), which may reflect transient increases in ocean oxygen and nutrient availability that permitted greater body size and morphological complexity (Luo et al., 2025).

More broadly, enhanced weathering-driven eutrophication associated with LIP volcanism can influence ocean redox in markedly different ways depending on the prevailing background state. In the predominantly oxic Phanerozoic ocean, efficient aerobic remineralization means that productivity pulses typically accelerated oxygen consumption, promoting expanded anoxia and even contributing to mass extinction events (Schobben et al., 2020). These effects were further amplified under greenhouse conditions, which weakened deep water ventilation and limited oxygen resupply (Hotinski et al., 2001). In contrast, the Mesoproterozoic ocean was persistently low in oxygen with ferruginous deep waters (Poulton and Canfield, 2011). This strongly stratified redox structure likely reduced remineralization efficiency at depth. As a result, nutrient-driven productivity sustained over longer ($\geq 10^5$ – 10^6 yr) timescales could have enhanced organic carbon burial efficiency and produced a net gain in surface-ocean O_2 , even if local respiration intensified. These contrasting responses highlight how the environmental impacts of volcanism and enhanced weathering depend on the background redox state of the contemporaneous Earth System and on the balance between the timescales of oxygen production and consumption, offering key insights into the environmental controls on the coevolution of life and the Earth System during Earth's middle age.

5. Conclusion

Our study presents the first evidence of a coupled positive Sr and Li isotope excursion in early Mesoproterozoic seawater, revealing a significant weathering event at approximately 1.57 Ga. This event was characterised by an increased chemical weathering rate alongside decreased weathering congruency. We propose that the onset of this weathering pulse was primarily driven by elevated CO_2 emissions from intense volcanic activity, possibly accompanied by orogenic uplift and erosion. Enhanced weathering increased the delivery of nutrients and sulfate to the ocean, stimulating the burial of organic carbon and pyrite, and potentially contributing to a pulse of ocean oxygenation. This pulsed oxygenation event may have created more favourable conditions for the emergence and radiation of the earliest known, decimetre-scale, multicellular eukaryotic organisms during the early Mesoproterozoic Era.

Funding

This study was supported from the Natural Environment Research Council (NERC) (NE/P013643/1 (BETR programme) to G.A.S., Y.Z. and S.W.P.; and NE/R010129/1 to G.A.S., S.W.P. and P.A.E.P.v.S.); the National Key Research and Development Program of China (2022YFF0800100); the National Natural Science Foundation of China (41921002) to M.Z.; and the Dean's Prize of the Faculty of Mathematical and Physical Sciences (UCL) to X.C.

Author contributions

X.C., Y.Z., and G.A.S. conceived and designed the study. X.C. and Y.Z.

developed the methodology. F.T.B., C.M., S.Z., M.Z., and D.L. carried out the investigation and data collection. X.C. and F.T.B. prepared the visualizations. Y.Z. and G.A.S. supervised the research. X.C. wrote the original draft of the manuscript. All authors contributed to reviewing and editing the manuscript, including X.C., Y.Z., S.W.P., F.T.B., C.M., S.Z., M.Z., D.L., P.A.E.P.v.S., B.J.W.M., and G.A.S.

CRediT authorship contribution statement

Xi Chen: Writing – review & editing, Writing – original draft, Methodology, Investigation, Conceptualization. **Ying Zhou:** Writing – review & editing, Supervision, Methodology, Investigation, Conceptualization. **Simon W. Poulton:** Writing – review & editing, Investigation, Funding acquisition. **Fred T. Bowyer:** Writing – review & editing, Investigation. **Colin Mettam:** Writing – review & editing, Investigation. **Shihong Zhang:** Writing – review & editing. **Maoyan Zhu:** Writing – review & editing. **Da Li:** Writing – review & editing, Investigation. **Philip A.E. Pogge von Strandmann:** Writing – review & editing, Funding acquisition. **Benjamin J.W. Mills:** Writing – review & editing. **Graham A. Shields:** Writing – review & editing, Supervision, Investigation, Funding acquisition.

Declaration of competing interest

The authors declare that they have no known competing financial interests or personal relationships that could have appeared to influence the work reported in this paper.

Acknowledgments

We appreciate D. Wilson and T. Gernon for valuable suggestions, and C. Liu, X. Liu and W. Shi for helpful discussions. We sincerely thank Dr Tristan J Horner for his editorial handling, and two anonymous reviewers for their constructive suggestions, which have significantly improved the manuscript. We acknowledge our much respected colleague and co-author, Shihong Zhang, who passes away during the course of this work and whose contribution to this study were highly significant.

Supplementary materials

Supplementary material associated with this article can be found, in the online version, at [doi:10.1016/j.epsl.2026.119848](https://doi.org/10.1016/j.epsl.2026.119848).

Data availability

All data has been included in the Supplementary Datasheet

References

- Alcott, L.J., Mills, B.J.W., Bekker, A., Poulton, S.W., 2022. Earth's great oxidation event facilitated by the rise of sedimentary phosphorus recycling. *Nat. Geosci.* 15. <https://doi.org/10.1038/s41561-022-00906-5> v.
- Baratoux, L., et al., 2019. New U–Pb baddeleyite ages of mafic dyke swarms of the west African and amazonian cratons: implication for their configuration in supercontinents through time. *Springer Geology*. <https://doi.org/10.1007/978-981-13-1666-1-7>.
- Bartley, J.K., Kah, L.C., 2004. Marine carbon reservoir, Corg–Ccarb coupling, and the evolution of the Proterozoic carbon cycle. *Geology* 32. <https://doi.org/10.1130/G19939.1> v.
- Basu, A.R., Jacobsen, S.B., Poreda, R.J., Dowling, C.B., Aggarwal, P.K., 2001. Large groundwater strontium flux to the oceans from the Bengal basin and the marine strontium isotope record. *Science* 293. <https://doi.org/10.1126/science.1060524> v.
- Bataille, C.P., Willis, A., Yang, X., Liu, X., 2017. Continental igneous rock composition: a major control of past global chemical weathering. *Sci. Adv.* 3, 1–16 [ve1602183](https://doi.org/10.1126/sciadv.1602183).
- Bellefroid, E.J., Planavsky, N.J., Miller, N.R., Brand, U., Wang, C., 2018. Case studies on the utility of sequential carbonate leaching for radiogenic strontium isotope analysis. *Chem. Geol.* 497, 88–99. <https://doi.org/10.1016/j.chemgeo.2018.08.025> v.
- Berner, R.A., 2003. The long-term carbon cycle, fossil fuels and atmospheric composition. *Nature* 426. <https://doi.org/10.1038/nature02131>.

- Brasier, M.D., Lindsay, J.F., 1998. A billion years of environmental stability and the emergence of eukaryotes: new data from northern Australia. *Geology* 26. [https://doi.org/10.1130/0091-7613\(1998\)026<0555:ABY0ES>2.3.CO;2](https://doi.org/10.1130/0091-7613(1998)026<0555:ABY0ES>2.3.CO;2) v.
- Brocks, J.J., Nettersheim, B.J., Adam, P., Schaeffer, P., Jarrett, A.J.M., Güneli, N., Liyanage, T., van Maldegem, L.M., Hallmann, C., Hope, J.M., 2023. Lost world of complex life and the late rise of the eukaryotic crown. *Nature* 618. <https://doi.org/10.1038/s41586-023-06170-w> v.
- Broecker, W.S., and Peng, T.H., 1983. Tracers in the sea.: [doi:10.1016/0016-7037\(83\)90075-3](https://doi.org/10.1016/0016-7037(83)90075-3).
- Butterfield, N.J., 2015. Early evolution of the Eukaryota. *Palaeontology* 58. <https://doi.org/10.1111/pala.12139> v.
- Butterfield, N.J., 2009. Oxygen, animals and oceanic ventilation: an alternative view. *Geobiology* 7. <https://doi.org/10.1111/j.1472-4669.2009.00188.x> v.
- Canfield, D.E., Zhang, S., Frank, A.B., Wang, X., Wang, H., Su, J., Ye, Y., Frei, R., 2018. Highly fractionated chromium isotopes in Mesoproterozoic-aged shales and atmospheric oxygen. *Nat. Commun.* 9. <https://doi.org/10.1038/s41467-018-05263-9> v.
- Cao, C., Bataille, C.P., Song, H., Saltzman, M.R., Tierney Cramer, K., Wu, H., Korte, C., Zhang, Z., Liu, X.M., 2022. Persistent late Permian to early Triassic warmth linked to enhanced reverse weathering. *Nat. Geosci.* 15. <https://doi.org/10.1038/s41561-022-01009-x> v.
- Caves Rugenstein, J.K., Ibarra, D.E., von Blanckenburg, F., 2019. Neogene cooling driven by land surface reactivity rather than increased weathering fluxes. *Nature* 571, 99–102. <https://doi.org/10.1038/s41586-019-1332-y> v.
- Cawood, P.A., Hawkesworth, C.J., 2014. Earth's middle age. *Geology* 42, 503–506. <https://doi.org/10.1130/G35402.1> v.
- Chan, L.H., Edmond, J.M., Thompson, G., Gillis, K., 1992. Lithium isotopic composition of submarine basalts: implications for the lithium cycle in the oceans. *Earth Planet. Sci. Lett.* 108. [https://doi.org/10.1016/0012-821X\(92\)90067-6](https://doi.org/10.1016/0012-821X(92)90067-6) v.
- Chen, B., et al., 2022a. A short-lived oxidation event during the early Ediacaran and delayed oxygenation of the Proterozoic ocean. *Earth Planet. Sci. Lett.* 577. <https://doi.org/10.1016/j.epsl.2021.117274> v.
- Chen, X., Zhou, Y., 2023. Effective leaching of argillaceous and dolomitic carbonate rocks for strontium isotope stratigraphy. *Geostand. Geanalytical Res.* 48. <https://doi.org/10.1111/ggr.12531>.
- Chen, X., Zhou, Y., Bowyer, F., Mettam, C., Zhang, K., Shields, G.A., 2025. Evaluating the utility of rare earth elements as a redox proxy: a case study from the c. 1.57 Ga Gaoyuzhuang formation, North China Craton. *J. Geol. Soc. jgs2025–jgs2183*. <https://doi.org/10.1144/jgs2025-183>.
- Chen, X., Zhou, Y., Shields, G.A., 2022b. Progress towards an improved Precambrian seawater $87\text{Sr}/86\text{Sr}$ curve. *Earth-Sci. Rev.* 224. <https://doi.org/10.1016/j.earscirev.2021.103869> v.
- Condie, K.C., 2021. Revisiting the Mesoproterozoic. *Gondwana Res.* 100, 44–52. <https://doi.org/10.1016/j.gr.2020.08.001> v.
- Condie, K.C., Pisarevsky, S.A., Puetz, S.J., Roberts, N.M.W., Spencer, C.J., 2023. A-type granites in space and time: relationship to the supercontinent cycle and mantle events. *Earth Planet. Sci. Lett.* 610. <https://doi.org/10.1016/j.epsl.2023.118125> v.
- Coogan, L.A., Dosso, S., 2012. An internally consistent, probabilistic, determination of ridge-axis hydrothermal fluxes from basalt-hosted systems. *Earth Planet. Sci. Lett.* 323–324. <https://doi.org/10.1016/j.epsl.2012.01.017> v.
- Daines, S.J., Mills, B.J.W., Lenton, T.M., 2017. Atmospheric oxygen regulation at low Proterozoic levels by incomplete oxidative weathering of sedimentary organic carbon. *Nat. Commun.* 8. <https://doi.org/10.1038/ncomms14379> v.
- Day, C.C., Pogge von Strandmann, P.A.E., Mason, A.J., 2021. Lithium isotopes and partition coefficients in inorganic carbonates: proxy calibration for weathering reconstruction. *Geochim. Cosmochim. Acta* 305. <https://doi.org/10.1016/j.gca.2021.02.037> v.
- Dellinger, M., Gaillardet, J., Bouchez, J., Calmels, D., Louvat, P., Dosseto, A., Gorge, C., Alanoca, L., Maurice, L., 2015. Riverine Li isotope fractionation in the Amazon River basin controlled by the weathering regimes. *Geochim. Cosmochim. Acta* 164, 71–93. <https://doi.org/10.1016/j.gca.2015.04.042> v.
- Diamond, C.W., Ernst, R.E., Zhang, S.H., and Lyons, T.W., 2021. Breaking the boring billion: a case for solid-earth processes as drivers of system-scale environmental variability during the mid-Proterozoic, in *Large Igneous Provinces: A Driver of Global Environmental and Biotic Changes*, [doi:10.1002/9781119507444.ch21](https://doi.org/10.1002/9781119507444.ch21).
- Dodd, M.S., et al., 2023. Uncovering the Ediacaran phosphorus cycle. *Nature* 617. <https://doi.org/10.1038/s41586-023-06077-6>.
- Elderfield, H., 1986. Strontium isotope stratigraphy. *Palaeogeogr. Palaeoclimatol. Palaeoecol.* 57. [https://doi.org/10.1016/0031-0182\(86\)90007-6](https://doi.org/10.1016/0031-0182(86)90007-6).
- Gervais, F., Beaudry, A., Kavanagh-Lepage, C., Moukhsil, A., Larson, K.P., Guilmette, C., 2023. Far from boring: a new Grenvillian perspective on Mesoproterozoic tectonics. *Earth Planet. Sci. Lett.* 610. <https://doi.org/10.1016/j.epsl.2023.118129> v.
- Guo, H., Du, Y., Kah, L.C., Hu, C., Huang, J., Huang, H., Yu, W., Song, H., 2015. Sulfur isotope composition of carbonate-associated sulfate from the Mesoproterozoic Jixian Group, North China: implications for the marine sulfur cycle. *Precambrian Res.* 266. <https://doi.org/10.1016/j.precamres.2015.05.032> v.
- Guo, H., Du, Y., Kah, L.C., Huang, J., Hu, C., Huang, H., Yu, W., 2013. Isotopic composition of organic and inorganic carbon from the Mesoproterozoic Jixian group, North China: implications for biological and oceanic evolution. *Precambrian Res.* 266. <https://doi.org/10.1016/j.precamres.2012.09.023>.
- Habicht, K.S., Gade, M., Thamdrup, B., Berg, P., Canfield, D.E., 2002. Calibration of sulfate levels in the Archean ocean. *Science* 298. <https://doi.org/10.1126/science.1078265> v.
- Halverson, G.P., Wade, B.P., Hurtgen, M.T., Barovich, K.M., 2010. Neoproterozoic chemostratigraphy. *Precambrian Res.* 182. <https://doi.org/10.1016/j.precamres.2010.04.007>.
- Holland, H.D., 2006. The oxygenation of the atmosphere and oceans. *Philos. Trans. R. Soc. B* 316. <https://doi.org/10.1098/rstb.2006.1838>.
- Hotinski, R.M., Bice, K.L., Kump, L.R., Najjar, R.G., Arthur, R.G., 2001. Ocean stagnation and end-Permian anoxia. *Geology* 29, 7–10. [https://doi.org/10.1130/0091-7613\(2001\)029<0007:OSAEP>2.0.CO;2](https://doi.org/10.1130/0091-7613(2001)029<0007:OSAEP>2.0.CO;2) v.
- Huh, Y., Chan, L.H., Zhang, L., Edmond, J.M., 1998. Lithium and its isotopes in major world rivers: implications for weathering and the oceanic budget. *Geochim. Cosmochim. Acta* 62. [https://doi.org/10.1016/S0016-7037\(98\)00126-4](https://doi.org/10.1016/S0016-7037(98)00126-4).
- Isson, T.T., Planavsky, N.J., 2018. Reverse weathering as a long-term stabilizer of marine pH and planetary climate. *Nature* 560. <https://doi.org/10.1038/s41586-018-0408-4>.
- Jeffcoate, A.B., Elliott, T., Thomas, A., Bouman, C., 2004. Precise, small sample size determinations of lithium isotopic compositions of geological reference materials and modern seawater by MC-ICP-MS. *Geostand. Geanalytical Res.* 28. <https://doi.org/10.1111/j.1751-908X.2004.tb01053.x> v.
- Kalderon-Asael, B., et al., 2021. A lithium-isotope perspective on the evolution of carbon and silicon cycles. *Nature* 595. <https://doi.org/10.1038/s41586-021-03612-1> v.
- Krause, A.J., Sluijs, A., van der Ploeg, R., Lenton, T.M., Pogge von Strandmann, P.A.E., 2023. Enhanced clay formation key in sustaining the Middle Eocene Climatic Optimum. *Nat. Geosci.* 16. <https://doi.org/10.1038/s41561-023-01234-y> v.
- Krissansen-Totton, J., Catling, D.C., 2020. A coupled carbon-silicon cycle model over Earth history: reverse weathering as a possible explanation of a warm mid-Proterozoic climate. *Earth Planet. Sci. Lett.* 537, 116181. <https://doi.org/10.1016/j.epsl.2020.116181> v.
- Kuznetsov, A.B., Semikhatov, M.A., Gorokhov, I.M., 2012. The Sr isotope composition of the world ocean, marginal and inland seas: implications for the Sr isotope stratigraphy. *Stratigr. Geol. Correl.* 20. <https://doi.org/10.1134/S0869593812060044> v.
- Li, X., et al., 2025. Isotopic evidence for oceanic barium cycling in the initial stage of the Mesoproterozoic. *Earth Planet. Sci. Lett.* 658, 119314. <https://doi.org/10.1016/j.epsl.2025.119314> v.
- Li, G., West, A.J., 2014. Evolution of Cenozoic seawater lithium isotopes: coupling of global denudation regime and shifting seawater sinks. *Earth Planet. Sci. Lett.* 401. <https://doi.org/10.1016/j.epsl.2014.06.011> v.
- Li, H., Zhu, S., Xiang, Z., Su, W., Lu, S., Zhou, H., Geng, J., Li, S., Yang, F., 2010. Zircon U-Pb dating on tuff bed from Gaoyuzhuang formation in Yanqing, Beijing: further constraints on the new subdivision of the Mesoproterozoic stratigraphy in the northern North China Craton. *Acta Petrol. Sin.* 26, 2131–2140 v.
- Liu, C.Y., Pogge von Strandmann, P.A.E., Tarbuck, C., Wilson, D.J., 2022a. Experimental investigation of oxide leaching methods for Li isotopes. *Geostand. Geanalytical Res.* 46. <https://doi.org/10.1111/ggr.12441> v.
- Liu, G., Zhang, S., Li, H., Bao, X., Zhao, H., Liang, D., Wu, H., Tang, D., Zhu, X., Yang, T., 2022b. Cyclostratigraphic calibration of the ca. 1.56 Ga carbon isotope excursion and oxygenation event recorded in the Gaoyuzhuang formation, north China. *Glob. Planet. Change* 216. <https://doi.org/10.1016/j.gloplacha.2022.103916> v.
- Liu, K., Zhang, S., Wang, X., Ye, Y., Zhang, P., Xiao, W., Liu, Y., Lyu, Y., 2025. Lithium isotope evidence for enhanced continental weathering at ~1.4 Ga. *Geophys. Res. Lett.* 52, e2024GL114218. <https://doi.org/10.1029/2024GL114218> v.
- Lu, Z., Jenkyns, H.C., Rickaby, R.E.M., 2010. Iodine to calcium ratios in marine carbonate as a paleo-redox proxy during oceanic anoxic events. *Geology* 38. <https://doi.org/10.1130/G31145.1> v.
- Lu, S., Yang, C., Li, H., Li, H., 2002. A group of rifting events in the terminal paleoproterozoic in the North China Craton. *Gondwana Res.*, 5. [https://doi.org/10.1016/s1342-937x\(05\)70896-0](https://doi.org/10.1016/s1342-937x(05)70896-0).
- Luo, J., Long, X., Bowyer, F., Poulton, S., 2020. Pulsed oxygenation events preceded progressive oxygenation of the early Mesoproterozoic ocean. *Earth Planet. Sci. Lett.* 559, 1656. <https://doi.org/10.46427/gold2020.1656> v.
- Luo, J., Poulton, S.W., Chen, B., Miao, L., Chen, K., Sun, H., Wang, Z., Li, G., Zhu, M., 2025. High-resolution chemostratigraphy reveals a large $\delta^{13}\text{C}$ gradient in the ~1.56 Ga redox-stratified ocean. *Precambrian Res.* 422, 107785. <https://doi.org/10.1016/J.PRECAMRES.2025.107785> v.
- Luo, A., Sun, G., Grasby, S.E., Yin, R., 2024. Large igneous provinces played a major role in oceanic oxygenation events during the mid-Proterozoic. *Commun. Earth Environ.* 5, 609. <https://doi.org/10.1038/s43247-024-01780-2> v.
- Magna, T., Wiechert, U.H., Halliday, A.N., 2004. Low-blank isotope ratio measurement of small samples of lithium using multiple-collector ICPMS. *Int. J. Mass Spectrom.* 239. <https://doi.org/10.1016/j.ijms.2004.09.008> v.
- Marriott, C.S., Henderson, G.M., Crompton, R., Staubwasser, M., Shaw, S., 2004. Effect of mineralogy, salinity, and temperature on Li/Ca and Li isotope composition of calcium carbonate. *Chem. Geol.* 212. <https://doi.org/10.1016/j.chemgeo.2004.08.002> v.
- McArthur, J.M., 1994. Recent trends in strontium isotope stratigraphy. *Terra Nova* 6. <https://doi.org/10.1111/j.1365-3121.1994.tb00507.x>.
- Mei, M., 2006. Origin of molar-tooth structure based on sequence-stratigraphic position and macroscopic features: example from Mesoproterozoic Gaoyuzhuang formation at Jixian Section, Tianjin, North China. *J. China Univ. Geosci.* 17. [https://doi.org/10.1016/S1002-0705\(06\)60029-0](https://doi.org/10.1016/S1002-0705(06)60029-0) v.
- Misra, S., Froelich, P.N., 2012. Lithium isotope history of Cenozoic seawater: changes in silicate weathering and reverse weathering. *Science* 335, 818–823. <https://doi.org/10.1126/science.1214697> v.
- Nana Yobo, L., Brandon, A.D., Holmden, C., Lau, K.V., Eldrett, J., 2021. Changing inputs of continental and submarine weathering sources of Sr to the oceans during OAE 2. *Geochim. Cosmochim. Acta* 303. <https://doi.org/10.1016/j.gca.2021.03.013> v.
- Oze, C., Sleep, N.H., Coleman, R.G., Fendorf, S., 2016. Anoxic oxidation of chromium. *Geology* 44, 543–546. <https://doi.org/10.1130/G37844.1> v.

- Peucker-Ehrenbrink, B., Fiske, G.J., 2019. A continental perspective of the seawater $^{87}\text{Sr}/^{86}\text{Sr}$ record: a review. *Chem. Geol.* 510, 140–165. <https://doi.org/10.1016/j.chemgeo.2019.01.017> v.
- Pogge von Strandmann, P.A.E., Dellinger, M., West, A.J., 2021a. Lithium isotopes: a tracer of past and present silicate weathering. *Elem. Geochem. Tracers Earth Syst. Sci.*
- Pogge von Strandmann, P.A.E., Henderson, G.M., 2015. The Li isotope response to mountain uplift. *Geology* 43, 67–70. <https://doi.org/10.1130/G36162.1> v.
- Pogge von Strandmann, P.A.E., Jenkyns, H.C., Woodfine, R.G., 2013. Lithium isotope evidence for enhanced weathering during Oceanic Anoxic Event 2. *Nat. Geosci.* 6. <https://doi.org/10.1038/ngeo1875> v.
- Pogge von Strandmann, P.A.E., Jones, M.T., Joshua West, A., Murphy, M.J., Stokke, E. W., Tarbuck, G., Wilson, D.J., Pearce, C.R., Schmidt, D.N., 2021b. Lithium isotope evidence for enhanced weathering and erosion during the Paleocene-Eocene thermal maximum. *Sci. Adv.* 7. <https://doi.org/10.1126/sciadv.abb4224> v.
- Pogge von Strandmann, P.A.E., Schmidt, D.N., Planavsky, N.J., Wei, G., Todd, C.L., Baumann, K.H., 2019. Assessing bulk carbonates as archives for seawater Li isotope ratios. *Chem. Geol.* 530, 119338. <https://doi.org/10.1016/j.chemgeo.2019.119338> v.
- Porter, S.M., 2020. Insights into eukaryogenesis from the fossil record. *Interface Focus* 10, 20190105. <https://doi.org/10.1098/rsfs.2019.0105> v.
- Poulton, S.W., Canfield, D.E., 2011. Ferruginous conditions: a dominant feature of the ocean through Earth's history. *Elements* 7. <https://doi.org/10.2113/gselements.7.2.107> v.
- Pourteau, A., Smit, M.A., Li, Z.X., Collins, W.J., Nordsvan, A.R., Volante, S., Li, J., 2018. 1.6 Ga crustal thickening along the final Nuna suture. *Geology* 46, 959–962. <https://doi.org/10.1130/G45198.1> v.
- Richter, F.M., Liang, Y., 1993. The rate and consequences of Sr diagenesis in deep-sea carbonates. *Earth Planet. Sci. Lett.* 117. [https://doi.org/10.1016/0012-821X\(93\)90102-F](https://doi.org/10.1016/0012-821X(93)90102-F) v.
- Richter, F.M., Rowley, D.B., DePaolo, D.J., 1992. Sr isotope evolution of seawater: the role of tectonics. *Earth Planet. Sci. Lett.* 109, 11–23. [https://doi.org/10.1016/0012-821X\(92\)90070-C](https://doi.org/10.1016/0012-821X(92)90070-C) v.
- Richter, F.M., Turekian, K.K., 1993. Simple models for the geochemical response of the ocean to climatic and tectonic forcing. *Earth Planet. Sci. Lett.* 119. [https://doi.org/10.1016/0012-821X\(93\)90010-7](https://doi.org/10.1016/0012-821X(93)90010-7) v.
- Rothman, D.H., Hayes, J.M., Summons, R.E., 2003. Dynamics of the Neoproterozoic carbon cycle. *Proc. Natl. Acad. Sci. U. S. A.* 100. <https://doi.org/10.1073/pnas.0832439100>.
- Runnegar, B., 1991. Precambrian oxygen levels estimated from the biochemistry and physiology of early eukaryotes. *Palaeogeogr. Palaeoclimatol. Palaeoecol.* 97, 97–111. [https://doi.org/10.1016/0031-0182\(91\)90186-U](https://doi.org/10.1016/0031-0182(91)90186-U) v.
- Saad, E.M., Wang, X., Planavsky, N.J., Reinhard, C.T., Tang, Y., 2017. Redox-independent chromium isotope fractionation induced by ligand-promoted dissolution. *Nat. Commun.* 8, 1590. <https://doi.org/10.1038/s41467-017-01694-y> v.
- Schlager, W., 2010. Ordered hierarchy versus scale invariance in sequence stratigraphy. *Int. J. Earth Sci.* 99, 139–151. <https://doi.org/10.1007/s00531-009-0491-8> v.
- Schobben, M., et al., 2020. A nutrient control on marine anoxia during the end-Permian mass extinction. *Nat. Geosci.* 13, 640–646. <https://doi.org/10.1038/s41561-020-0622-1> v.
- Shang, M., Tang, D., Shi, X., Zhou, L., Zhou, X., Song, H., Jiang, G., 2019. A pulse of oxygen increase in the early Mesoproterozoic ocean at ca. 1.57–1.56 Ga. *Earth Planet. Sci. Lett.* 527, 115797. <https://doi.org/10.1016/j.epsl.2019.115797> v.
- Shi, W., Mills, B.J.W., Li, C., Poulton, S.W., Krause, A.J., He, T., Zhou, Y., Cheng, M., Shields, G.A., 2022. Decoupled oxygenation of the Ediacaran ocean and atmosphere during the rise of early animals. *Earth Planet. Sci. Lett.* 591. <https://doi.org/10.1016/j.epsl.2022.117619> v.
- Shields, G., 2007. A normalised seawater strontium isotope curve: possible implications for Neoproterozoic-Cambrian weathering rates and the further oxygenation of the Earth. *eEarth* 2, 35–42. <https://doi.org/10.5194/ee-2-35-2007> v.
- Shields, G.A., Mills, B.J.W., Zhu, M., Raub, T.D., Daines, S.J., Lenton, T.M., 2019. Unique Neoproterozoic carbon isotope excursions sustained by coupled evaporite dissolution and pyrite burial. *Nat. Geosci.* 12, 823–827. <https://doi.org/10.1038/s41561-019-0434-3> v.
- Shields, G., Veizer, J., 2002. Precambrian marine carbonate isotope database: version 1.1. *Geochem. Geophys. Geosystems* 3. <https://doi.org/10.1029/2001GC000266> v.
- Song, K., Li, D., Lv, Y.W., Yuan, C., Qu, Y.R., Liu, S.A., 2024. Zinc isotope evidence for enhanced organic carbon burial driving transient oxygenation of the Mesoproterozoic ocean. *Precambrian Res.* 406, 107398. <https://doi.org/10.1016/J.PRECAMRES.2024.107398> v.
- Sperling, E.A., Frieder, C.A., Raman, A.V., Girguis, P.R., Levin, L.A., Knoll, A.H., 2013. Oxygen, ecology, and the Cambrian radiation of animals. *Proc. Natl. Acad. Sci. U. S. A.* 110. <https://doi.org/10.1073/pnas.1312778110> v.
- Spooner, E.T.C., 1976. The strontium isotopic composition of seawater, and seawater-oceanic crust interaction. *Earth Planet. Sci. Lett.* 31. [https://doi.org/10.1016/0012-821X\(76\)90108-4](https://doi.org/10.1016/0012-821X(76)90108-4).
- Tajika, E., Matsui, T., 1992. Evolution of terrestrial proto-CO₂ atmosphere coupled with thermal history of the earth. *Earth Planet. Sci. Lett.* 113. [https://doi.org/10.1016/0012-821X\(92\)90223-1](https://doi.org/10.1016/0012-821X(92)90223-1) v.
- Tang, D., et al., 2022. Enhanced weathering triggered the transient oxygenation event at ~1.57 Ga. *Geophys. Res. Lett.* 49. <https://doi.org/10.1029/2022GL099018> v.
- Teixeira, W., Reis, N.J., Bettencourt, J.S., Klein, E.L., and Oliveira, D.C., 2019, Intraplate proterozoic magmatism in the amazonian craton reviewed: geochronology, crustal tectonics and global barcode matches, in Springer *Geology*, doi:10.1007/978-981-13-1666-1_4.
- Tessier, I., Campbell, P.G.C., Bisson, M., 1979. Sequential extraction procedure for the speciation of particulate trace metals. *Anal. Chem.* 51. <https://doi.org/10.1021/ac50043a017> v.
- Tian, H., et al., 2015. Zircon LA-MC-ICPMS U-Pb dating of tuff from Mesoproterozoic Gaoyuzhuang formation in Jixian County of North China and its geological significance. *Acta Geosci. Sin.* 36, 647–658 v.
- Walker, J.C.G., Hays, P.B., Kasting, J.F., 1981. A negative feedback mechanism for the long-term stabilization of Earth's surface temperature. *J. Geophys. Res.* 86. <https://doi.org/10.1029/JC086iC10p09776>.
- Wang, C., et al., 2021. Chromium isotope systematics and the diagenesis of marine carbonates. *Earth Planet. Sci. Lett.* 562, 116824. <https://doi.org/10.1016/J.EPSL.2021.116824> v.
- Weis, D., et al., 2006. High-precision isotopic characterization of USGS reference materials by TIMS and MC-ICP-MS. *Geochem. Geophys. Geosystems* 7. <https://doi.org/10.1029/2006GC001283> v.
- West, A.J., Galy, A., Bickle, M., 2005. Tectonic and climatic controls on silicate weathering. *Earth Planet. Sci. Lett.* 235. <https://doi.org/10.1016/j.epsl.2005.03.020> v.
- Workman, R.K., Hart, S.R., 2005. Major and trace element composition of the depleted MORB mantle (DMM). *Earth Planet. Sci. Lett.* 231. <https://doi.org/10.1016/j.epsl.2004.12.005>.
- Xie, B., et al., 2024. Elevated phosphorus concentrations in shallow oceans as a trigger for the 1.57-Ga oxygenation event. *Geophys. Res. Lett.* 51, e2024GL111586. <https://doi.org/10.1029/2024GL111586> v.
- Xie, B., Zhu, J.ming, Wang, X., Xu, D., Zhou, L., Zhou, X., Shi, X., Tang, D., 2023. Mesoproterozoic oxygenation event: from shallow marine to atmosphere. *Bull. Geol. Soc. Am.* 135. <https://doi.org/10.1130/B36407.1> v.
- Xu, D., Qin, Z., Wang, X., Li, J., Shi, X., Tang, D., Liu, J., 2023. Extensive sea-floor oxygenation during the early Mesoproterozoic. *Geochim. Cosmochim. Acta* 354. <https://doi.org/10.1016/j.gca.2023.06.007> v.
- Yang, C., Guo, H., Huang, H., Hou, M., Luo, A., Yin, R., 2025. Large volcanism, enhanced oceanic productivity, and efficient organic matter burial during Mesoproterozoic oxygenation events: insights from mercury and carbon isotopes in the Jixian group, North China Craton. *Chem. Geol.* 695, 123052. <https://doi.org/10.1016/J.CHEMGEO.2025.123052> v.
- Zhang, T., Li, M., Chen, X., Wang, T., Shen, Y., 2022. High atmospheric CO₂ levels in the early Mesoproterozoic estimated from paired carbon isotopic records from carbonates from North China. *Precambrian Res.* 380. <https://doi.org/10.1016/j.precamres.2022.106812> v.
- Zhang, S., Li, Z.X., Evans, D.A.D., Wu, H., Li, H., Dong, J., 2012. Pre-Rodinia supercontinent Nuna shaping up: a global synthesis with new paleomagnetic results from North China. *Earth Planet. Sci. Lett.* 353–354. <https://doi.org/10.1016/j.epsl.2012.07.034> v.
- Zhang, S., Wang, H., Wang, X., Zheng, W., Hao, J., Pogge von Strandmann, P.A.E., Ye, Y., Shi, M., Liu, Y., Lyu, Y., 2025. Subaerial volcanism broke mid-Proterozoic environmental stasis. *Sci. Adv.* 10, eadk5991. <https://doi.org/10.1126/sciadv.adk5991> v.
- Zhang, K., Zhu, X., Wood, R.A., Shi, Y., Gao, Z., Poulton, S.W., 2018. Oxygenation of the Mesoproterozoic ocean and the evolution of complex eukaryotes. *Nat. Geosci.* 11, 345–350. <https://doi.org/10.1038/s41561-018-0111-y> v.
- Zhu, S., Zhu, M., Knoll, A.H., Yin, Z., Zhao, F., Sun, S., Qu, Y., Shi, M., Liu, H., 2016. Decimetre-scale multicellular eukaryotes from the 1.56-billion-year-old Gaoyuzhuang formation in North China. *Nat. Commun.* 7. <https://doi.org/10.1038/ncomms11500> v.